J. Fluid Mech. (2026), *vol.* 1034, A48, doi:10.1017/jfm.2026.11509

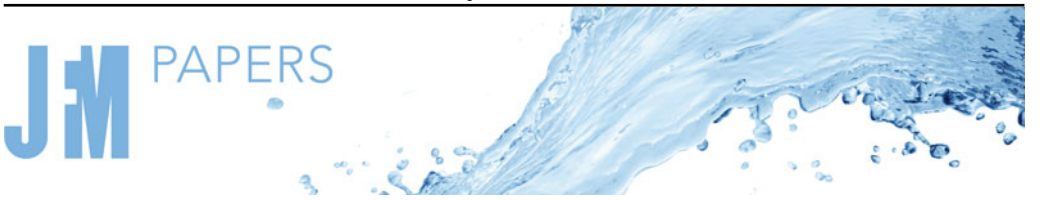

Oblique shocks in shallow flows of power-law fluids past abrupt channel deviations

Andrea Baroni[1], **Michele Iervolino**[2], **Luca Chiapponi**[3], **Cristiana Di Cristo**[4], **Andrea Vacca**[4], **Sandro Longo**[3] and **Vittorio Di Federico**[1]

[1]Department of Civil, Chemical, Environmental and Materials Engineering, Alma Mater Studiorum Università di Bologna, Bologna, Italy

[2]Department of Engineering, Università degli Studi della Campania 'L. Vanvitelli', Aversa (CE), Italy

[3]Department of Engineering and Architecture, Università degli Studi di Parma, Parco Area delle Scienze 181/A, Parma 43124, Italy

[4]Department of Civil, Building and Environmental Engineering, Università degli Studi di Napoli 'Federico II', Napoli, Italy

Corresponding author: Vittorio Di Federico, vittorio.difederico@unibo.it

(Received 7 August 2025; revised 6 March 2026; accepted 30 March 2026)

Building on classical oblique jump theory, we develop a one-dimensional (1-D) analytical framework that incorporates non-Newtonian rheology to predict the onset of hydraulic jumps, their internal structure and the associated Mach-front geometry. Source terms representing bed slope and wall friction are included, and the resulting formulation is systematically assessed against laboratory experiments, two-dimensional (2-D) shallow-water simulations and fully three-dimensional (3-D) computational fluid dynamics. Experiments with Newtonian, shear-thinning and shear-thickening fluids on converging sidewalls demonstrate a good match with the 1-D formulation. For Newtonian and shear-thinning fluids on mild slopes, the 1-D formulation with source terms closely reproduces the measured shock-front geometry and the 2-D simulation results. The analysis shows that upstream flow deceleration governs the reduction of the Mach angle and the resulting curvature. By contrast, in tests with shear-thickening fluids and steeper slopes, gravitational contributions produce detachment and strong front curvature that are not captured by the 1-D model. Comparisons of the transverse front position confirm that 1-D models lose validity when the upstream Froude number decreases sharply along the front. Fully 3-D simulations reveal concave front deformation driven by shear, strong dominance of tangential over normal velocities and flow features absent in depth-averaged models. The results demonstrate that 2-D shallow-water models capture the key dynamics for mild

slopes and shear-thinning conditions, while accurate prediction for shear-thickening fluids requires 3-D approaches, motivating future hybrid strategies.

Key words: non-Newtonian flows, shallow water flows, shock waves

1. Introduction

A hydraulic jump occurs in the context of open-channel flow when a high-velocity, low-depth (supercritical) current transitions abruptly to a low-velocity, high-depth (subcritical) state. The transition is typically not smooth and is associated with energy dissipation. The main causes are: (i) a sudden increase in downstream depth; (ii) changes in channel geometry, such as an abrupt expansion in channel width, a drop in channel slope or an abrupt channel deviation; (iii) obstructions in the flow path induced by structures like weirs or sluice gates; (iv) abrupt decrease in bed slope; (v) a sudden increase in bed wall roughness; (vi) energy dissipation design, when a hydraulic jump is intentionally created in stilling basins to reduce flow energy; (vii) certain combinations of discharge, depth and channel shape leading to supercritical conditions that cannot be sustained, forcing a jump. An in-depth description of the hydraulic jump can be found in Bakhmeteff (1932) and Chow (1959), while more recent reviews are Chanson (2009) and De Padova & Mossa (2021).

Thus, a deflection of the channel axis, either abrupt or progressively curved, is a common cause of the hydraulic jump, especially in irrigation systems, such as the one considered in the pioneering study by Ippen (1936). The sudden increase in water depth due to hydraulic jump in a sudden deflection or progressive superelevation on the concave side of a bent channel can lead to overspilling, thus representing the main technical obstacle. Other interesting applications concern the field of granular flow, as shown by Wieland, Gray & Hutter (1999) and Gray & Cui (2007); in particular, this type of flow can be applied to model snow avalanches, like in Cui, Gray & Johannesson (2007)'s case.

The earliest investigations into rapid flow within deflected channels were conducted by Prandtl (1931), Busemann (1931), Riabouchinsky (1932), Riabouchinsky (1934) and Preiswerk (1938) who emphasized the analogy between such flows and the supersonic gas dynamics, introducing a graphical solution method based on characteristic curves. Von Kármán (1938) derived an expression for the increase in water depth along the concave side of a channel bend, assuming constant specific energy. In contrast, Ippen (1936), Ippen & Knapp (1936) and Knapp & Ippen (1938) addressed the same problem under the assumption of constant velocity, leading to a different analytical solution. The specific case of an oblique hydraulic jump resulting from an abrupt channel deflection was first introduced by Rouse (1938) and Ippen (1943). A comprehensive review of earlier studies is provided by Citrini (1940), Citrini (1950), Rouse (1959), Chow (1959), Levi (1965) and Press & Schröder (1966).

Ippen (1936) conducted one of the most complete experimental investigations on supercritical flow in curved channels. His work was later complemented by Engelund & Munch-Petersen (1953), who analysed wave formation in converging and diverging channels. Poggi (1956) performed a series of experiments in a curved channel to validate the analytical models proposed by Ippen (1936) and von Kármán (1938). The Poggi findings were subsequently referenced in the laboratory studies of Sananes & Acatay (1962) and Reinauer & Hager (1997). Finally, Marchi (1988) presented experimental results for the limiting case of an abrupt 90° channel bend, with further references to his work appearing in Solari & Dey (2016).

More recently, Hager *et al.* (1994) conducted a series of experimental tests, supported by numerical results based on a shallow-water framework. In a similar vein, Causon, Mingham & Ingram (1999) used shallow-water numerical simulations to evaluate the increase in depth of the water caused by an oblique shock wave. Beltrami, Repetto & Del Guzzo (2007) conducted experiments with the practical aim of reducing superelevation near the channel wall and regularizing flow by installing water flaps along the wall.

The hydraulic jump in Newtonian fluids has been extensively studied, whereas research on non-Newtonian rheologies remains comparatively limited. A seminal study by Ng & Mei (1994) examined the properties and evolution of roll waves in power-law fluids, also theoretically analysed in Longo (2011).

Regarding fluid characterization, Haldenwang & Slatter (2006) and Burger, Haldenwang & Alderman (2010*a*) compiled valuable experimental databases detailing the rheological behaviour of non-Newtonian fluids, specifically in straight channels with varying cross-sectional geometries.

In direct connection with hydraulic jumps, Shu & Zhou (2006) and Zhou, Shu & Stansby (2007) investigated these phenomena in Bingham fluids flowing through straight channels. Unlike the classical Newtonian case, where analytical solutions for conjugate depths are readily available, their analysis led to systems of nonlinear algebraic equations, which required numerical methods for resolution. To address this, they proposed approximate formulae for estimating conjugate depths, thereby offering practical tools for engineering applications involving non-Newtonian flows. A similar methodology was adopted by Ugarelli & Di Federico (2007) for Herschel–Bulkley fluids, including an example application based on experimental data from Haldenwang & Slatter (2006), regarding the flow of a 6 % kaolin suspension down an inclined rectangular flume.

More recently, Samanta *et al.* (2022, 2023) presented analytical, numerical and experimental studies on hydraulic jumps in power-law fluids under planar conditions, using a shallow-water framework. Their approach was extended to Bingham plastics in Samanta *et al.* (2024*a*) and to Herschel–Bulkley fluids in Samanta *et al.* (2024*b*). Finally, Wang, Khayat & De Bruin (2023) extended the analysis to Herschel–Bulkley fluids in circular geometries. However, to the authors' knowledge, a comprehensive investigation of laminar hydraulic jumps in non-Newtonian fluids flowing through channels with abrupt deviations has yet to be undertaken. This gap is particularly notable given the relevance of such flows in environmental applications, such as modelling mud flows (Cui *et al.* 2007), the conveyance or disposal of mine tailings in industrial waste management (Burger *et al.* 2010*b*), landslides, debris and lava flows. Furthermore, non-Newtonian fluids are prevalent in a wide range of industrial processes where deviations in free-surface channels may arise, including cooling and coating processes (Chimetta & Franklin 2023), foam cleaning (Dallagi *et al.* 2022) and food science in general (Mathijssen *et al.* 2023).

In this study, the laminar free-surface flow of a power-law (Ostwald–de Waele) fluid – the simplest and most widely used non-Newtonian rheological model – is examined in the presence of a geometric disturbance, namely an abrupt angular channel deflection, which can induce the formation of a hydraulic jump. Although idealized, the power-law model effectively captures the rheological behaviour of clay–water mixtures commonly found in natural settings such as landslides (Carotenuto *et al.* 2015), estuarine muds (Zhang *et al.* 2020) and mine tailings (Borger 2013). Field-scale applications of laminar flows adopting a power-law rheology have been reported by Haldenwang & Slatter (2006) for bentonite and kaolin suspensions and carboxymethylcellulose solutions, by Latkovic & Levy (1991) for fluidized magnetite powder, by Kozic *et al.* (2016) for soybean paste and by Kumbár *et al.* (2021) for chocolate masses. Another example of laminar free-surface flow of a non-Newtonian fluid without yield-stress is provided by human and animal blood

(Horner, Wagner & Beris 2021) or silicon-like material in injection moulding (Chiappini 2020). Nevertheless, both assumptions of power-law rheology and laminar flow constitute limitations of the present work.

In the first case, many natural and industrial fluids, as well as contaminants, exhibit finite yield stress, with a rheological behaviour more accurately described by Bingham or Herschel–Bulkley constitutive models.

In the second case, it will be of considerable interest in future work to investigate the behaviour of non-Newtonian fluids in a transitional and fully turbulent regime. The evolution of their flow fields from laminar through transition to turbulence at high Reynolds numbers remains an open research problem. Significant differences are known to exist compared with Newtonian turbulence, and this area still requires fundamental investigation. For example, Guzel *et al.* (2009) reported pronounced asymmetries in turbulent puffs that were attributed to fluid rheology, although the mean flow was perfectly axisymmetric.

The overarching objective is to investigate the conditions leading to the formation and structure of hydraulic jumps in these flows, and more generally, to characterize the development of oblique shocks that include proper hydraulic jumps as a special case. To this end, three secondary objectives are pursued: (i) the development of a one-dimensional (1-D) analytical framework, based on the governing equations of mass conservation, momentum balance and power-law rheology, following the classical formulations by Ippen (1936) and von Kármán (1938); (ii) the design and execution of controlled laboratory experiments in inclined, laterally deflected channels aimed at observing the conditions for jump formation, the shock structures and the geometry of the Mach front (whether rectilinear or curved, detached or attached), preceded by rheological characterization of the fluid properties; (iii) extensive numerical simulations of diverse flow configurations, employing both a depth-averaged shallow-water model and a depth-resolved multiphase solver implemented in OpenFOAM.

The paper is organized as follows. Section 2 presents the geometrical set-up and simplified 1-D formulation of the problem, leading to the rheological equation and the uniform velocity profile. In § 3, a simplified flow analysis is conducted based on conservation principles, resulting in a nonlinear transcendental system of three algebraic equations with three unknowns. Section 4 details the laboratory experiments conducted in a tilted, laterally deflected channel. Numerical simulations are presented in § 5: a shallow-water formulation verifying experimental tests is presented first, then it is used to ascertain the validity of a 1-D formulation incorporating friction and bed slope. Section 6 illustrates the results of a depth-resolved solver implemented in OpenFOAM. A summary and comparative analysis of the results obtained from the analytical, experimental and numerical approaches is provided in § 7, which also includes conclusions and perspectives for future work.

2. One-dimensional formulation

A wide rectangular horizontal channel conveying an Ostwald–de Waele (hereafter power-law) fluid in a steady laminar regime undergoes an abrupt deflection of its axis by an angle θ, causing a perturbation of the flow conditions, as shown in figure 1. Variation in flow conditions occurs only downstream of a perturbation wave, originating at the vertex of the deflection and inclined by the Mach angle β from the wall (Press & Schröder 1966). The upstream and downstream conditions, indicated, respectively, with subscripts 1 and 2, are connected by this wavefront.

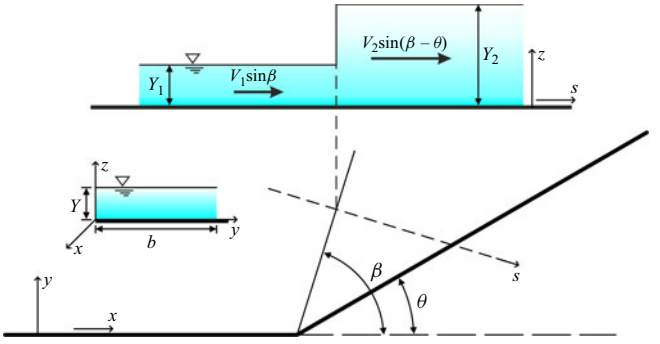

Figure 1. Geometry of the deflected channel and representation of the shock wave.

For a rectangular channel with depth Y along the vertical z-direction (using the conventional hydraulic engineering notation Y for depth, to ensure consistency with the literature and with the notation adopted in subsequent sections) where $Y \ll b$ (lubrication approximation) and b is the channel width in the transverse y-direction, the transverse and vertical velocity components are negligible and the velocity vector is approximately $\boldsymbol{u} = (u, 0, 0)$ as $\tau_{yx} \ll \tau_{zx}$, where u is the velocity in the x direction, τ_{yx} and τ_{zx} are components of the shear stress tensor. The hydrostatic pressure distribution is also assumed, consistent with the lubrication approximation adopted earlier. Under these conditions, the rheological equation for a power-law fluid simplifies to the following 1-D form:

$$\tau_{zx} = -K \left| \frac{\partial u}{\partial z} \right|^{n-1} \frac{\partial u}{\partial z}, \tag{2.1}$$

where K and n are the consistency index and the fluid behaviour index, respectively. For $n < 1$, the fluid is shear-thinning (pseudoplastic); for $n = 1$, the fluid is Newtonian and K reduces to μ, the dynamic viscosity; for $n > 1$, the fluid is shear-thickening (dilatant).

The channel is considered to have negligible wall and bottom effects; the velocity varies along the vertical, from a minimum at the bottom to a maximum at the free surface, with a distribution given by the following equation (Di Federico 1998):

$$u(z) = u_{max} \left[1 - \left(1 - \frac{z}{Y} \right)^{\frac{n+1}{n}} \right], \tag{2.2}$$

where u_{max} is the maximum velocity value at the free surface. The average velocity V in the x direction is obtained by integrating the previous equation along the vertical direction z, resulting in

$$V = \frac{1}{Y} \int_0^Y u(z)\, \mathrm{d}z = \left(\frac{n+1}{2n+1} \right) u_{max}. \tag{2.3}$$

The Boussinesq coefficient C_M, also termed the dimensionless momentum flux correction coefficient or shape factor, which accounts for the non-uniformity of the velocity profile in the vertical direction, can be calculated for a power-law fluid from (2.2) as (Ng & Mei 1994)

$$C_M = \frac{\int_A u^2 \, \mathrm{d}A}{A \left(\frac{1}{A} \int_A u \, \mathrm{d}A \right)^2} = \frac{2(2n+1)}{3n+2}, \tag{2.4}$$

where A is the cross-sectional area.

The problem studied here involves the determination of three unknowns: the depth of the downstream flow Y_2, the angle of Mach β and the average downstream velocity V_2. The known quantities are the depth of the upstream flow Y_1, the mean velocity V_1, the angle of deflection of the channel θ and the rheological parameters K and n. Flow conditions are conveniently characterized in terms of the Froude number Fr:

$$Fr = \frac{V}{\sqrt{gY}} = \left(\frac{n+1}{2n+1}\right)\frac{u_{max}}{\sqrt{gY}}, \tag{2.5}$$

where g is the gravity. The Boussinesq coefficient C_M defined in (2.4) is directly correlated to the critical Froude number Fr_c for an Ostwald–de Waele fluid (Campomaggiore *et al.* 2016), through the expression

$$Fr_C = 1/\sqrt{C_M}. \tag{2.6}$$

For convenience in the subsequent analysis, we introduce the normalized Froude number $F_* = Fr/Fr_c = Fr\sqrt{C_M}$, i.e. the ratio of the Froude number to the critical Froude number.

It should be noted that in cases where the velocity profile in the vertical direction can be approximated as uniform, i.e. $C_M = 1$, such as in turbulent clear water flows (Ippen 1936) or dense granular flows (Gray & Cui 2007), the critical Froude number equals unity ($Fr_c = 1$), and thus F_{*1} coincides with the Froude number Fr_1. In contrast, for laminar flows of power-law fluids, the critical Froude number varies depending on the rheological properties of the fluid, specifically the power-law exponent n.

2.1. *Criterion for laminar flow*

The criterion adopted here to verify the laminar flow follows the empirical method proposed by Darby (1986) and subsequently applied by Ng & Mei (1994). The flow is considered laminar if the wide-channel Reynolds number, defined as

$$Re = \frac{\rho V^{2-n} Y^n}{K}, \tag{2.7}$$

where ρ is the density of the fluid, remaining below the critical threshold

$$Re_c = 0.125\left(\frac{3n+1}{2n}\right)^n [2100 + 875(1-n)]\,. \tag{2.8}$$

3. Solution to the 1-D formulation

3.1. *Analytical solution based on mass and momentum balance*

In the geometry presented in § 2 where the channel axis undergoes an abrupt deflection, the flow dynamics can be described by a system of three governing equations (Levi 1965). The first is the continuity equation, written per unit width and projected normal to the wavefront, reading as

$$\int_0^{Y_1} u_1(z)\sin(\beta)\,\mathrm{d}z = \int_0^{Y_2} u_2(z)\sin(\beta-\theta)\,\mathrm{d}z. \tag{3.1}$$

The second and third equations derive from the momentum balance expressed along normal and parallel directions to the wavefront, respectively, assuming a hydrostatic pressure distribution $p = \rho g(Y - z)$; these two projections can be written as

$$\int_0^{Y_2} \rho u_2^2(z)\sin^2(\beta-\theta)\,\mathrm{d}z - \int_0^{Y_1} \rho u_1^2(z)\sin^2(\beta)\,\mathrm{d}z = \int_0^{Y_1} p_1\,\mathrm{d}z - \int_0^{Y_2} p_2\,\mathrm{d}z, \tag{3.2}$$

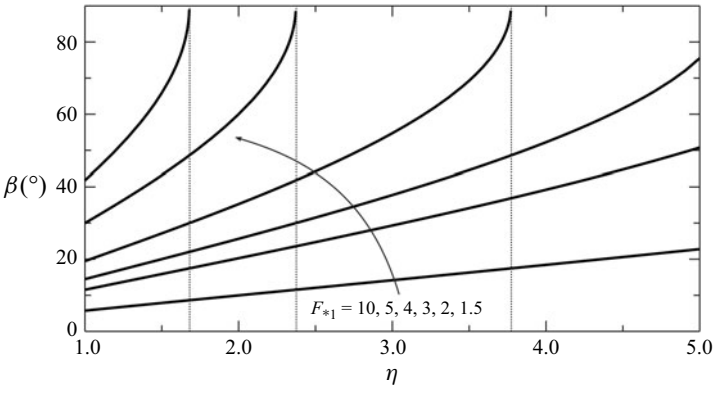

Figure 2. Mach angle β as a function of depth ratio η for various values of F_{*1}.

$$\int_0^{Y_1} u_1(z)\frac{1}{Y_1}\cos(\beta)\,\mathrm{d}z = \int_0^{Y_2} u_2(z)\frac{1}{Y_2}\cos(\beta-\theta)\,\mathrm{d}z. \tag{3.3}$$

It is convenient to define the following dimensionless ratios: $\zeta = V_2/V_1$ and $\eta = Y_2/Y_1$. By integrating the velocity profile given (2.2) the system of (3.1)–(3.3) can be solved. This yields a transcendental system of three equations that determines the unknown set (Y_2, V_2, β), given the geometric and rheological parameters of the flow:

$$\begin{cases} \zeta\eta = \dfrac{\sin(\beta)}{\sin(\beta-\theta)}, \\ \zeta = \dfrac{\cos(\beta)}{\cos(\beta-\theta)}, \\ \dfrac{1-\eta^2}{2Fr_1^2 C_M} = \zeta^2\eta\sin^2(\beta-\theta) - \sin^2(\beta). \end{cases} \tag{3.4}$$

In Appendix A, the system (3.4) is derived following the standard approach used in gas dynamics for the analysis of oblique shock waves.

From system (3.4) the following equation can be derived:

$$\sin^2(\beta) = \frac{\eta^2+\eta}{2Fr_1^2 C_M} = \frac{\eta^2+\eta}{2F_{*1}^2}. \tag{3.5}$$

The plot of the relationship $\eta-\beta$ in figure 2 reveals that at high values of F_{*1}, the depth ratio η increases rapidly with the Mach angle β. In contrast, for values of F_{*1} closer to unity, the increase in η with β is more gradual.

Equation (3.5) is a quadratic expression in η, which is solved by considering only the positive root, since η must be non-negative, i.e.

$$\eta = \frac{1}{2}\sqrt{1+8Fr_1^2 C_M\sin^2(\beta)} - \frac{1}{2}. \tag{3.6}$$

Furthermore, (3.1) and (3.3) can be combined as follows:

$$\eta = \frac{\tan(\beta)}{\tan(\beta-\theta)}. \tag{3.7}$$

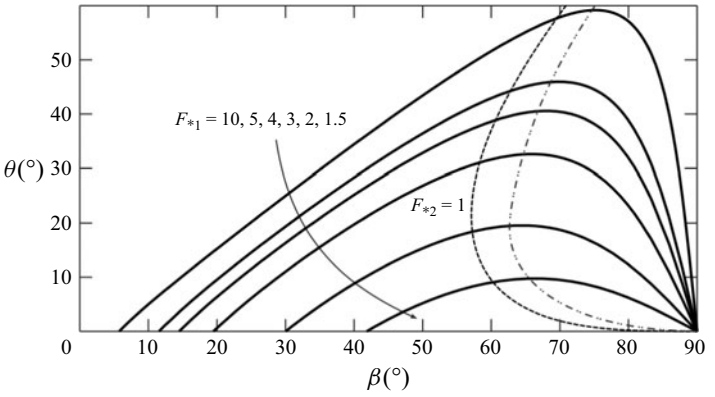

Figure 3. Mach angle β as a function of deflection angle θ for various values of F_{*1}; the dashed line at $F_{*2} = 1$ delineates the boundary between tranquil (subcritical) and rapid (supercritical) flow downstream; the dot-dashed line connects the maxima θ_{max} and identifies the point of detachment.

Substituting (3.6) into (3.7) yields a valuable relationship between the Mach angle β and the known flow conditions, channel geometry and fluid rheology:

$$\tan(\theta) = \frac{\tan(\beta)\left(3 - \sqrt{1 + 8Fr_1^2 C_M \sin^2(\beta)}\right)}{1 - 2\tan^2(\beta) - \sqrt{1 + 8Fr_1^2 C_M \sin^2(\beta)}}. \tag{3.8}$$

Figure 3 illustrates the relationship between the deflection angle θ and the Mach angle β for various values of F_{*1} upstream; the curve of β versus θ for given F_{*1} increases, reaches a maximum and decreases again; physically, this means that for known deflection angle θ and Froude number upstream, there are two possible values of β, one corresponding to a weak shock, the other to a strong shock. Note that by combining the continuity equation with the momentum equation projected normal to the shock (i.e. the first and third equations in (3.4)), and rearranging the resulting relations, one can express them in terms of the downstream Froude number Fr_2 as

$$\sin^2(\beta - \theta) = \frac{1 + \eta}{2\eta^2 Fr_2^2 C_M}, \tag{3.9}$$

which provides a convenient framework for analysing the downstream flow regime and to plot the critical curve $Fr_2 = Fr_c$ in figure 3. As shown in the figure, for a given deflection angle θ there are generally two possible values of β: one corresponds to a supercritical flow downstream and the other to a subcritical flow downstream; the coexistence of the latter with the supercritical flow upstream gives rise to a hydraulic jump.

Another feature, already pointed out by Ippen (1943) for inviscid flows and clearly illustrated in figure 3, is that for each value of Fr_1 upstream the θ-curve possesses a maximum θ_{max}. When, for a given Fr_1, the deflection angle θ exceeds this maximum, the shock is no longer attached to the point of wall deflection but propagates upstream, producing what is referred to as a detached shock. In this case, the disturbance takes the form of a curved perturbation wave. The location of these maxima can be determined by setting the derivative of θ with respect to β to zero. To this end, (3.8) can be rewritten as

$$\theta = \beta - \arctan\left[\frac{1 + \sqrt{1 + 8Fr_1^2 C_M \sin^2(\beta)}}{2Fr_1^2 C_M \sin(2\beta)}\right]. \tag{3.10}$$

Differentiating this relation with respect to β yields the value β_{max} corresponding to the maximum deflection angle θ_{max} for a given Fr_1. When θ exceeds this value, shock detachment occurs. The resulting expression leads to a quartic equation in $\sin^2(\beta_{max})$:

$$\begin{aligned} 16Fr_1^6C_M^3\sin^8(\beta_{max}) - &\left(32Fr_1^6C_M^3 + 6Fr_1^4C_M^2\right)\sin^6(\beta_{max}) \\ &+ \left(16Fr_1^6C_M^3 - 12Fr_1^4C_M^2\right)\sin^4(\beta_{max}) \\ &+ \left(10Fr_1^4C_M^2 + 5Fr_1^2C_M\right)\sin^2(\beta_{max}) + 1 + 2Fr_1^2C_M = 0. \end{aligned} \tag{3.11}$$

The above equation allows us, for a given value of the upstream Froude number Fr_1, to implicitly calculate β_{max} and determine whether the deflection is such as to induce the detachment. The curve connecting the maxima θ_{max}, obtained by plotting θ_{max} as a function of β_{max} according to (3.10), is depicted in figure 3, and can be considered as the criterion for the onset of detachment.

Furthermore, the momentum equation in the streamwise direction (3.7) can be rearranged to express it explicitly in terms of both Froude numbers as

$$\frac{Fr_2^2}{Fr_1^2} = \frac{\tan(\beta-\theta)}{\tan(\beta)}\left[\frac{1+\tan^2(\beta-\theta)}{1+\tan^2(\beta)}\right]. \tag{3.12}$$

By imposing $Fr_2 = Fr_c = 1/\sqrt{C_M}$ and replacing θ using the (3.10), the resulting expression can be manipulated to yield following the cubic equation in $\sin^2(\beta_{crit})$:

$$\begin{aligned} 4Fr_1^6C_M^3\sin^6(\beta_{crit}) - &\left(8Fr_1^6C_M^3 + 16Fr_1^4C_M^2\right)\sin^4(\beta_{crit}) \\ +&\left(8Fr_1^4C_M^2 + 6Fr_1^2C_M + 4Fr_1^6C_M^3\right)\sin^2(\beta_{crit}) + Fr_1^2C_M + 1 = 0. \end{aligned} \tag{3.13}$$

Solving this equation yields the value of β_{crit} associated with the critical flow condition. It is worth noting that, setting $C_M = 1$ in (3.11) and (3.13), the expressions reduce to those derived by Gray & Cui (2007) for a granular stream. Substituting β_{crit} into (3.8) directly yields the critical condition, indicating whether the flow passes from rapid to tranquil and produces a hydraulic jump.

In summary, the general validity of the system (3.4) enables the solution for a power-law fluid to be obtained by analogy with the classical case of a vertically uniform velocity profile (Ippen 1936), i.e. $C_M = 1$, provided that the Froude number is scaled by its corresponding critical value (the F_{*1} ratio).

Consequently, the analogy between oblique shocks in rapid free-surface flows, generated by an abrupt channel deflection, and those in gas dynamics, produced when a uniform gas stream encounters an inclined surface, extends naturally to power-law currents (Gray & Cui 2007). Based on the preceding analysis, three types of shock may arise in a steady rapid current of a power-law fluid when the channel is suddenly deflected. For sufficiently large upstream Froude numbers and small deflection angles θ, two shock angles β are possible (see figure 3): the larger angle corresponds to a strong shock, in which the downstream flow becomes subcritical ($Fr_2 < Fr_c$) and a hydraulic jump forms, while the smaller angle corresponds to a weak shock, in which the downstream flow remains supercritical ($Fr_2 > Fr_c$) and only a wavefront connects two distinct rapid-flow states. The onset of the more energetically dissipative strong shock is determined by downstream boundary conditions, which force the flow to become subcritical.

Furthermore, when the deflection angle exceeds the maximum value θ_{max} identified above, or when the upstream Froude number is not sufficiently large, an oblique shock solution to system (3.4) ceases to exist. Under these conditions, the shock detaches and takes a curved form (Ippen 1943). In turbulent flows of clear-water or granular free-surface flows, the occurrence of weak, strong and detached shocks depends solely on Fr_1 and θ.

By contrast, for laminar power-law fluids, rheological properties also influence the type of shock, since the governing parameters are the pair (F_{*1}, θ), where F_{*1} depends on the Boussinesq coefficient C_M and, consequently, on the fluid behaviour index n.

3.2. *Head loss*

The specific head (E) at any cross-section is defined as the sum of the flow depth (Y) and a kinetic energy term corrected for the non-uniform velocity distribution by the Coriolis coefficient α, also known as the kinetic energy correction factor. For a power-law fluid, α is given by

$$\alpha = \frac{\int_A u^3 \, \mathrm{d}A}{A\left(\frac{1}{A}\int_A u \, \mathrm{d}A\right)^3} = \frac{6(2n+1)^2}{(3n+2)(4n+3)}, \tag{3.14}$$

where u is the velocity, A is the cross-sectional area and n is the flow behaviour index.

Using this coefficient, the specific head is expressed as

$$E = Y + \alpha \frac{V^2}{2g}. \tag{3.15}$$

Hydraulic jump is a dissipative phenomenon characterized by localized energy loss, which can be quantified as the difference in the specific head between the upstream and downstream sections (Ugarelli & Di Federico 2007). The specific head loss ΔE (equal to the hydraulic head loss ΔH for a horizontal channel) is thus

$$\Delta E = E_1 - E_2 = Y_1 - Y_2 + \alpha \frac{V_1^2}{2g} - \alpha \frac{V_2^2}{2g}, \tag{3.16}$$

where subscripts 1 and 2 denote the upstream and downstream conditions, respectively.

Substituting the downstream velocity V_2 from the continuity equation and using the relationship given in (3.5), ΔE can be rewritten as

$$\Delta E = Y_1(1-\eta) + \alpha Y_1 Fr_1^2 \left[1 - \frac{\eta+1}{2\eta Fr_1^2 C_M} \frac{1}{\sin^2\left(\arcsin\sqrt{\frac{\eta^2+\eta}{2Fr_1^2 C_M}} - \theta\right)}\right]. \tag{3.17}$$

After some algebraic manipulations, (3.17) can be reformulated in a different form by eliminating the arcsine function to yield

$$\Delta E = Y_1(1-\eta) + \alpha Y_1 Fr_1^2 \left[1 - \frac{\eta+1}{2\eta Fr_1^2 C_M}\left(\cos(\theta)\sqrt{\frac{\eta^2+\eta}{2Fr_1^2 C_M}} - \sin(\theta)\sqrt{1 - \frac{\eta^2+\eta}{2Fr_1^2 C_M}}\right)^{-2}\right]. \tag{3.18}$$

Therefore, it is evident that head loss cannot be determined solely from upstream conditions; the downstream flow state also plays a role. Specifically, head loss ΔE depends on the upstream Froude number Fr_1 and flow depth Y_1, the fluid rheology characterized by the Boussinesq and Coriolis coefficients C_M and α, as well as on the downstream flow condition expressed by the fluid depth ratio η. Moreover, the geometry of the channel influences the loss of head through the deflection angle θ.

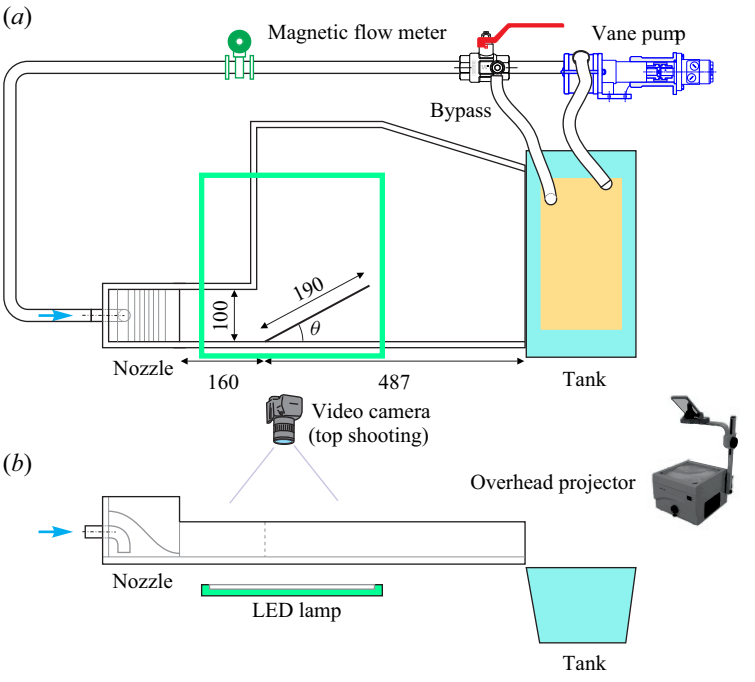

Figure 4. Experimental layout: (*a*) top view and (*b*) side view. A grid was projected onto the surface of the opaque shear-thickening fluid using an overhead projector. The channel bottom was inclined at 3.4°, except in the case of the shear-thickening fluid, where a steeper slope of 15° was required to achieve a sufficiently high Froude number for the incoming flow. Here LED denotes light-emitting diode.

In § 4, (3.18) will be used to calculate the head loss with experimental parameters. It will be evident that the case of a strong shock is more energetically dissipative than the weak one.

4. Experimental study

The following sections present and discuss the results of several experimental series conducted at the Hydraulic Laboratory of the University of Parma, preceded by a description of the experimental set-up. To the best of our knowledge, these experiments are novel, as no previous investigations have examined hydraulic jumps and oblique shocks induced by abrupt channel deflections in the viscous regime. By comparison, the most comprehensive earlier studies – those by Ippen (1936) – address turbulent flows on smooth channel bends.

The experiments were carried out in a transparent polymethyl methacrylate channel of width 100 mm that leads to a larger polymethyl methacrylate chamber (see figure 4). The channel was equipped with an adjustable partition that allowed for variation of the lateral wall angle. The details of the experimental set-up are given in the Supplementary material available at https://doi.org/10.1017/jfm.2026.11509.

Figure 5 presents snapshots of six experiments conducted over a range of increasing Froude numbers. In all cases, both the inlet and the outlet flows remained within the laminar regime. As the Froude number increased, the hydraulic jump structure became progressively more defined. At low Froude numbers, the jump displayed an undular shape, featuring two crests downstream of the channel corner. At very high Froude numbers, the jump evolved into a distinct wall jet.

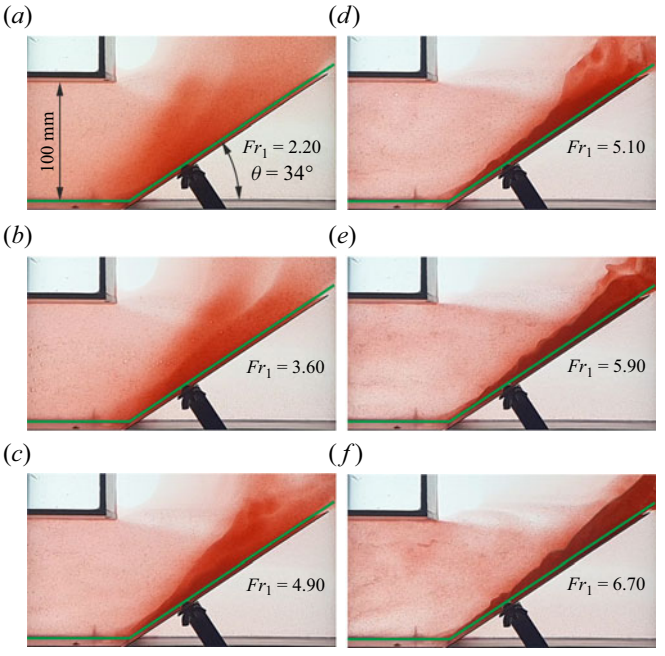

Figure 5. Snapshots from six experiments performed at a fixed sidewall deflection angle, showing the evolution of the hydraulic jump structure as the Froude number increases. The green lines represent the intersection between the bottom of the channel and the walls.

4.1. *Results of the experiments*

Table 1 provides an overview of the 44 experiments performed.

Three types of fluids were considered: (i) a strongly shear-thinning fluid with flow behaviour index $n < 1$; (ii) a Newtonian fluid with $n = 1$; (iii) a shear-thickening fluid with $n > 1$. Preliminary rheological tests on the shear-thinning mixtures indicated that their parameters remained nearly constant over time, confirming the good repeatability of the experiments. For Newtonian and shear-thickening fluids, two channel-deflection angles, $\theta = 15°$ and $25°$, were tested, while for shear-thinning fluids four angles were used, ranging from $15°$ to $34°$. Changing the flow rate Q, the upstream Froude number Fr_1 was established between 1.72 and 9.15, corresponding to the upstream Reynolds numbers Re_1 (calculated from (2.8) in § 2.1) in the range of 12–374. Figure 6 shows, for each fluid and for the two angles $\theta = 15°$ and $25°$, the experiment with the largest upstream Froude number.

An interesting application of (3.18) for the head loss is presented in table 2. For some selected experimental scenarios – only the weak shock case was experimentally obtained – the theoretical values of η and β for both weak and strong shock were calculated; obviously, the Mach angle and the downstream depth would have been higher in the latter case. As expected, the value of ΔE is much higher – almost an order of magnitude – for strong than for weak shocks; in fact, only in the latter case a proper hydraulic jump, a strongly dissipative phenomenon, takes place.

The uncertainty in the rheological parameters n and K arises mainly from three sources: the non-viscometric character of the flow conditions during rheometric testing; the inherent approximation involved in fitting the fluid behaviour to a power-law model; fluctuations in temperature throughout the measurement process. These combined factors produce relative uncertainties estimated at $\Delta n/n \leqslant 4\,\%$ and $\Delta K/K \leqslant 8\,\%$. Fluid

Test	n	k (Pa s^n)	ρ (kg m^{-3})	θ (°)	Fr_1	F_{*1}	$F_{*2,th}$	Re_1	$Re_{2,th}$	β_{exp} (°)	β_{th} (°)	η_{exp}	η_{th}
1	0.39	1.63	900	15	6.50	6.89	3.47	163	239	21.0	22.2	3.44	3.22
2	0.39	1.63	900	15	5.71	6.05	3.13	136	191	22.3	23.4	3.21	2.93
3	0.39	1.63	900	15	5.07	5.37	2.83	112	151	24.8	24.6	3.06	2.70
4	0.39	1.63	900	15	4.04	4.28	2.36	84	105	28.0	27.5	2.71	2.34
5	0.39	1.63	900	15	3.17	3.36	1.99	60	69	33.0	31.8	2.24	2.05
6	0.39	1.63	900	15	2.30	2.44	1.56	41	41	42.0	40.5	1.74	1.79
7	0.37	0.73	998	17	6.35	6.71	3.44	295	418	26.0	24.5	3.21	3.46
8	0.37	0.79	998	24	6.30	6.66	—	315	441	33.1	31.9	—	4.50
9	0.37	0.79	998	24	5.36	5.66	—	246	321	35.0	33.5	—	3.95
10	0.37	0.79	998	24	4.92	5.20	—	201	251	36.0	34.5	—	3.70
11	0.37	0.79	998	24	3.98	4.21	1.96	141	159	38.0	37.7	3.05	3.17
12	0.39	1.63	900	25	9.15	9.70	—	218	367	30.2	30.2	—	6.40
13	0.39	1.63	900	25	8.97	9.50	3.38	202	338	31.5	30.3	5.94	6.29
14	0.39	1.63	900	25	7.69	8.14	2.97	161	253	34.2	31.3	5.53	5.51
15	0.39	1.63	900	25	6.11	6.47	2.55	118	168	37.4	33.2	4.58	4.54
16	0.39	1.63	900	25	4.50	4.76	2.19	81	99	40.8	36.8	3.15	3.57
17	0.37	0.79	998	34	6.88	7.28	—	374	479	41.0	42.0	—	6.40
18	0.37	0.79	998	34	6.02	6.36	—	304	362	41.2	43.4	—	5.71
19	0.37	0.79	998	34	5.12	5.41	—	235	253	45.2	45.5	—	4.99
20	0.37	0.79	998	34	4.97	5.26	—	201	212	48.2	46.0	—	4.87
21	0.37	0.79	998	34	3.89	4.11	—	137	120	54.0	50.9	—	4.04
22	1.00	0.072	1213	15	6.29	6.89	—	155	527	20.8	22.2	—	3.22
23	1.00	0.072	1213	15	5.63	6.17	—	140	435	21.2	23.2	—	2.97
24	1.00	0.072	1213	15	4.92	5.39	2.89	124	351	22.0	24.6	2.94	2.71
25	1.00	0.072	1213	15	4.21	4.61	2.51	108	274	22.6	26.5	2.82	2.45
26	1.00	0.072	1213	15	3.48	3.81	2.15	92	206	24.0	29.4	2.53	2.19
27	1.00	0.072	1213	15	2.59	2.83	1.79	77	147	31.4	35.78	1.93	1.90
28	1.00	0.072	1213	25	5.23	5.73	2.41	109	420	33.4	34.5	3.95	4.11
29	1.00	0.072	1213	25	4.51	4.94	2.22	94	317	34.8	36.3	3.34	3.67
30	1.09	0.27	1563	15	5.14	5.64	2.78	31	104	25.2	24.1	3.51	2.80
31	1.09	0.25	1563	15	4.72	5.19	2.63	29	92	26.4	25.0	3.30	2.64
32	1.10	0.23	1563	15	4.05	4.45	2.37	26	74	27.2	27.0	2.92	2.40
33	1.10	0.21	1563	15	3.38	3.71	2.09	23	58	28.8	29.9	2.53	2.16
34	1.10	0.20	1563	15	2.83	3.11	1.85	20	46	31.0	33.5	2.18	1.98
35	1.10	0.20	1563	15	2.31	2.54	1.56	18	35	33.2	39.1	1.92	1.82
36	1.10	0.19	1563	15	1.94	2.13	1.32	15	28	37.4	46.0	1.73	1.72
37	1.09	0.24	1563	25	5.18	5.70	2.14	31	143	34.8	34.6	4.95	4.09
38	1.10	0.22	1563	25	4.83	5.31	2.05	28	124	34.6	35.4	4.61	3.88
39	1.10	0.20	1563	25	4.25	4.67	1.87	26	100	36.8	37.1	4.14	3.52
40	1.10	0.19	1563	25	3.60	3.95	1.65	23	77	37.0	40.0	3.62	3.13
41	1.10	0.18	1563	25	3.01	3.31	1.41	21	59	38.8	44.1	3.17	2.80
42	1.11	0.17	1563	25	2.50	2.75	1.17	18	43	43.0	50.5	2.73	2.54
43	1.11	0.16	1563	25	2.09	2.30	0.83	15	29	44.4	64.6	2.37	2.49
44	1.11	0.16	1563	25	1.72	1.89	0.83	12	22	45.2	63.3	2.12	2.10

Table 1. Parameters of the experimental tests. The symbols n, K and ρ denote the rheological index, consistency index and density of the fluid; θ is for the channel deflection angle; Fr_1 and Re_1 are for the upstream Froude and Reynolds numbers; F_{*1} and $F_{*2,th}$ are for the upstream and (theoretical) downstream normalized Froude number; $Re_{2,th}$ is for the theoretical downstream Reynolds number; β_{exp} and β_{th} are for the experimental and theoretical shock angles; and η_{exp} and η_{th} are for the experimental and theoretical ratios between downstream and upstream flow depth. The critical Reynolds number is $Re_c = 488$ for shear-thinning fluids, 525 for Newtonian fluids and 526 for shear-thickening fluids. The channel bed slope was 3.4° for shear-thinning and Newtonian fluids, and 15° for shear-thickening fluids. The gate opening height was $h_G = 5$ mm for shear-thinning and Newtonian fluids, and $h_G = 3$ mm for shear-thickening fluids.

Test	n	K (Pa s^n)	θ (°)	F_1^*	β_{th} (°)	η_{th}	ΔE (cm)
5*a*	0.39	1.63	15	3.36	2.05	31.8	0.87
5*b*	0.39	1.63	15	3.36	4.26	85.2	4.57
26*a*	1	0.072	15	3.81	2.19	29.4	1.18
26*b*	1	0.072	15	3.81	4.90	86.0	6.96
34*a*	1.1	0.2	15	3.11	1.98	33.5	0.56
34*b*	1.1	0.2	15	3.11	3.91	84.5	2.61

Table 2. Theoretical head loss ΔE for weak (letter *a*) and strong (letter *b*) shocks, calculated via (3.18) using the experimental parameters from cases 5, 26 and 34 from table 1.

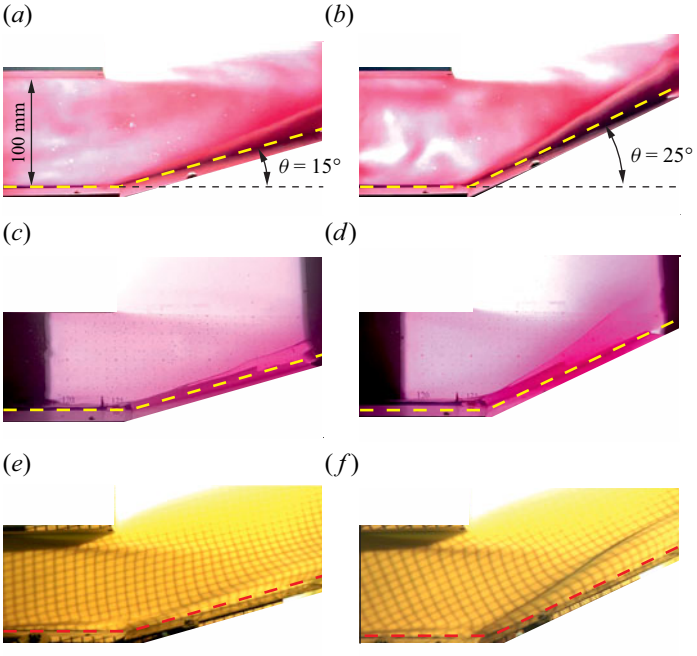

Figure 6. Snapshots from six representative experiments performed with three different fluids at wall deflection angles of 15° and 25°, illustrating the resulting hydraulic jump configurations. (*a*) Test 1, shear-thinning fluid, $Fr_1 = 6.50$; (*b*) Test 12, shear-thinning fluid, $Fr_1 = 9.15$; (*c*) Test 22, Newtonian fluid, $Fr_1 = 6.29$; (*d*) Test 28, Newtonian fluid, $Fr_1 = 5.23$; (*e*) Test 30, shear-thickening fluid, $Fr_1 = 5.14$; (*f*) Test 37, shear-thickening fluid, $Fr_1 = 5.18$. The dashed lines represent the intersection between the bottom of the channel and the walls.

density measurements were conducted with high precision; however, minor variations in temperature contribute to a conservative uncertainty estimate of $\Delta\rho/\rho \leqslant 0.2\,\%$.

The free-surface depth measurements upstream (Y_1) and downstream (Y_2) of the hydraulic jump were subject to experimental errors arising from measurement resolution and surface disturbances, with relative uncertainties quantified as $\Delta Y_1/Y_1 \leqslant 7\,\%$ and $\Delta Y_2/Y_2 \leqslant 3\,\%$, respectively. These combine to yield an uncertainty on the experimentally determined depth ratio $\eta_{exp} = Y_2/Y_1$ of up to $\Delta\eta_{exp}/\eta_{exp} \leqslant 10\,\%$.

Discharge Q was measured using a calibrated flow meter, resulting in a relative uncertainty $\Delta Q/Q \leqslant 1\,\%$. An additional systematic error is associated with the channel width b, estimated to be within ± 1 mm (that is, $\Delta b/b \leqslant 1\,\%$), which propagates into the calculation of the upstream Froude number Fr_1, contributing to the uncertainty

$\Delta Fr_1/Fr_1 \leqslant 13\,\%$. The propagation of uncertainty for a function of several parameters and variables is obtained through a first-order Taylor series expansion, in which the variances of all independent arguments are linearly combined. Further details can be found in Longo *et al.* (2013).

To estimate the Mach angle β_{exp}, the images were processed to extract the pixels corresponding to the jump front using a colour-based thresholding approach. A straight line was then fitted to these pixels, and the procedure was repeated over several tens of frames, with the resulting angles subsequently averaged. This method yields a result comparable to drawing a best-fit line by eye. Altering the colour threshold modifies the detected front primarily through translation and, to a much lesser extent, rotation. The uncertainty derived from this procedure therefore reflects the intrinsic variability within the ensemble of measured shock angles. The estimated uncertainty of $\Delta\beta_{exp}/\beta_{exp} \leqslant 5\,\%$, accounts for the uncertainty described previously and for the resolution limits of the images.

To estimate the uncertainty in the theoretical depth ratio η_{th}, a Monte Carlo simulation was performed. In this approach, the input parameters – namely the upstream Froude number Fr_1, the power-law exponent n and the channel deflection angle θ – were treated as independent random variables, each assumed to follow a normal distribution centred on its nominal value and with a standard deviation corresponding to its respective uncertainty. For the deflection angle, a standard deviation of $\Delta\theta = 0.1^\circ$ was assumed. By propagating these uncertainties through the governing equations, it was found that the resulting relative uncertainty in η_{th} is $\Delta\eta_{th}/\eta_{th} \leqslant 11\,\%$.

In addition, the uncertainty in the Reynolds number Re_1 was evaluated, which yielded a relative error estimate of $\Delta Re_1/Re_1 \leqslant 21\,\%$.

Figure 7 compares the theoretical and experimental Mach angles in varying Froude numbers for shear-thinning, Newtonian and shear-thickening fluids. The overall agreement is satisfactory, with the experimental error bars generally encompassing the theoretical predictions. Nevertheless, for Newtonian fluids – and, to a lesser degree, shear-thickening fluids – the theoretical Mach angles consistently overpredict the values observed experimentally.

Figure 8 presents a comparison between the experimental and theoretical values of η for the cases where the downstream depth Y_2 was measurable. The agreement is particularly good at higher η values, corresponding to larger Fr_1. At lower Fr_1, accurate measurement of Y_2 is challenging due to the surface undulations associated with the hydraulic jump. Other techniques could be used to measure Y_2, which will form part of our future activities on this topic. Given that the experimental activity was planned with a balance of resources and objectives in mind, and with the measurement of angle β in view, our focus was on achieving this objective.

Discrepancies between the theoretical and experimental values of η become pronounced again at very high Froude numbers, where the flow forms a jet impinging on the channel wall. This generates a highly curved flow structure that deviates significantly from the hydrostatic pressure distribution assumed in the theoretical model (see figure 9). Extending the length of the inclined wall and increasing the channel width may facilitate the development of a flow field that is more consistent with the theoretical assumptions, potentially improving the agreement between predictions and observations. The range of parameter combinations explored in the experiments listed in table 1 is considered adequate for validating the proposed models. Some limitations on the maximum attainable Froude number arise from the nature of the fluids used. In particular, shear-thinning fluids experience rapid degradation of the polymer chains responsible for their pseudoplastic behaviour when subjected to very high shear rates, which in our tests correspond to

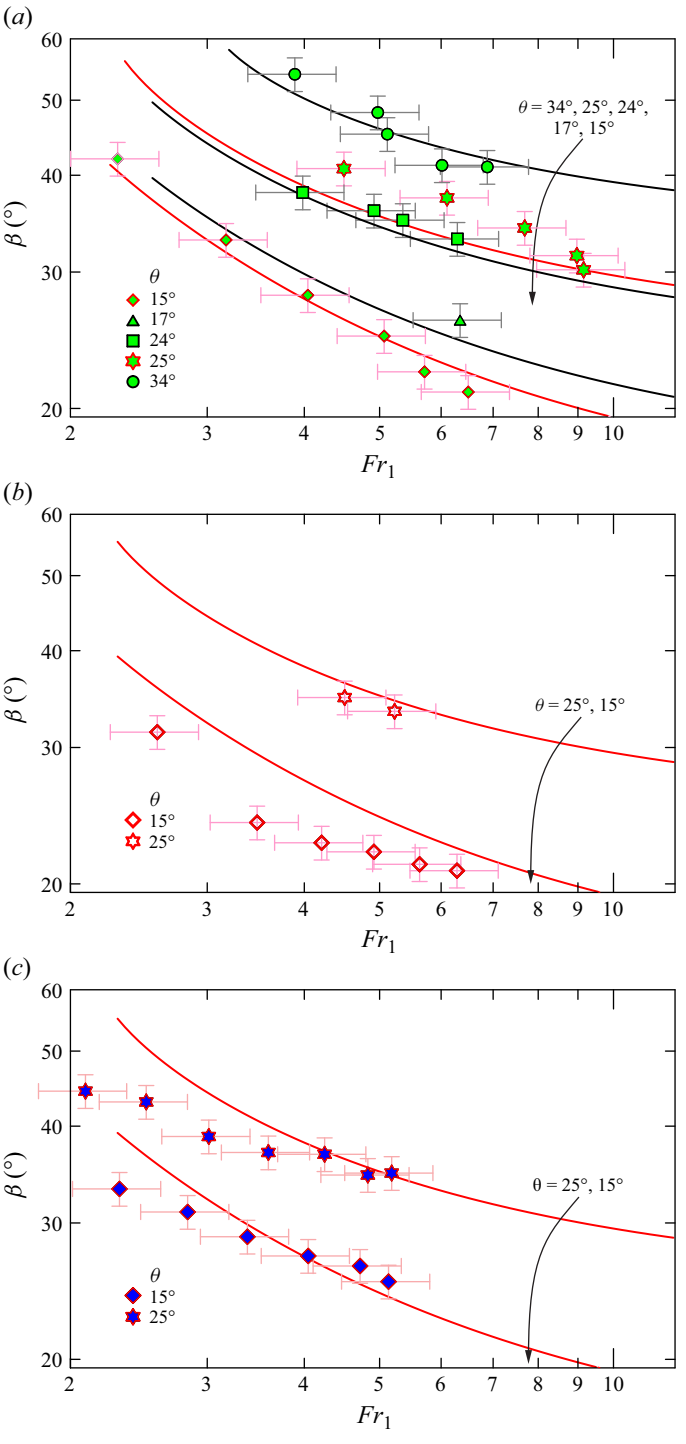

Figure 7. Comparison of the experimental Mach angle. (*a*) Shear-thinning fluid, (*b*) Newtonian fluid and (*c*) Shear-thickening fluid. Symbols are the experiments, curves are the theoretical values. Error bars refer to ±1 standard deviation.

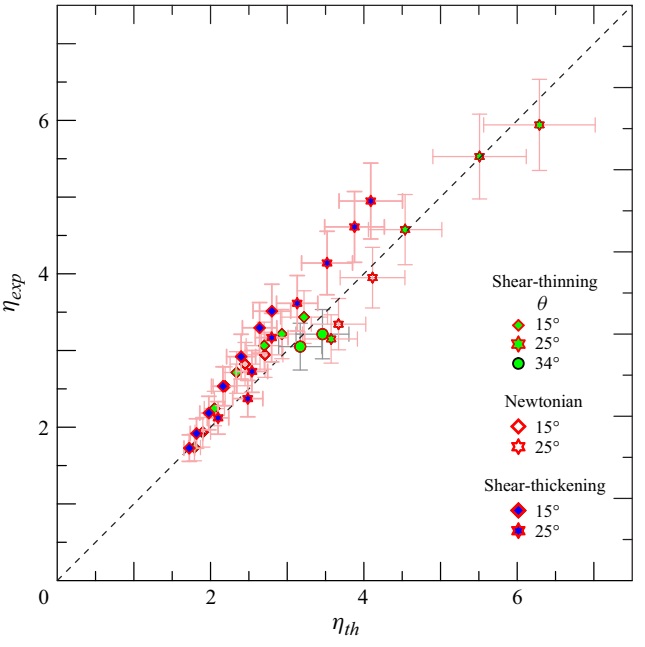

Figure 8. Comparison between experimental measurements and theoretical predictions of the depth ratio η. Error bars refer to ± 1 standard deviation.

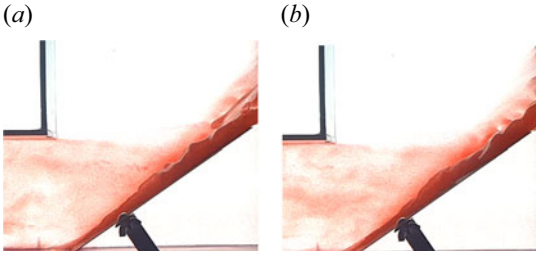

Figure 9. The jump evolves in a jet-like manner at very high Froude numbers. Test 17, shear-thinning fluid with $Fr_1 = 6.88$. Panels (*a*) and (*b*) are taken 1/8 of a second apart.

large Froude numbers. We acknowledge, however, that drawing more conclusive insights into the characteristics of the shocks would have benefited from a broader range of test conditions. Nevertheless, the selected experimental conditions span a sufficiently broad range of rheological behaviours and flow regimes – from subcritical to strongly supercritical – thus ensuring a meaningful validation of the models under diverse hydraulic conditions.

5. Two-dimensional shallow-water model

5.1. *Governing equations and numerical set-up*

We consider for generality the two-dimensional (2-D) depth-averaged mass and momentum conservation equations for a power-law fluid flowing over a gently inclined

(x, y) plane, reading, respectively, as

$$\frac{\partial Y}{\partial t} + \frac{\partial \left(V_x Y\right)}{\partial x} + \frac{\partial \left(V_y Y\right)}{\partial y} = 0, \tag{5.1}$$

$$\frac{\partial \left(V_x Y\right)}{\partial t} + \frac{\partial \left(C_M\, V_x V_x Y\right)}{\partial x} + \frac{\partial \left(C_M\, V_x V_y Y\right)}{\partial y} + \frac{\partial}{\partial x}\left(\frac{g Y^2}{2}\right) = S_x, \tag{5.2}$$

$$\frac{\partial \left(V_y Y\right)}{\partial t} + \frac{\partial \left(C_M\, V_x V_y Y\right)}{\partial x} + \frac{\partial \left(C_M\, V_y V_y Y\right)}{\partial y} + \frac{\partial}{\partial y}\left(\frac{g Y^2}{2}\right) = S_y, \tag{5.3}$$

where t denotes time; V_x and V_y are the velocity components averaged by depth in the x and y directions, respectively; C_M is the Boussinesq coefficient defined in (2.4). The source terms S_x and S_y incorporate the effects of the bottom slope and the basal shear stress, and are given by

$$S_x = g\, Y\, S_{0x} - \frac{K}{\rho}\left(\frac{2n+1}{n}\frac{1}{Y}\right)^n \left(V_x^2 + V_y^2\right)^{\frac{n-1}{2}} V_x, \tag{5.4}$$

$$S_y = g\, Y\, S_{0y} - \frac{K}{\rho}\left(\frac{2n+1}{n}\frac{1}{Y}\right)^n \left(V_x^2 + V_y^2\right)^{\frac{n-1}{2}} V_y, \tag{5.5}$$

with S_{0x} and S_{0y} representing the bottom slopes along the x and y directions, respectively.

Equations (5.1)–(5.3) extend the 1-D model of Ng & Mei (1994) to two dimensions (Greco *et al.* 2019; Yu & Chu 2022), assuming vertical accelerations to be negligible and adopting a hydrostatic distribution of the pressure (Hogg & Pritchard 2004).

The flow model (5.1)–(5.5) belongs to a class of models in the literature often referred to as the Saint–Venant approach, boundary-layer or lubrication approximation, and similar frameworks (Ancey 2007). The primary advantage of the Saint–Venant approach is that it enables the analysis of the flowing layer dynamics without requiring detailed knowledge of the internal flow structure. However, this simplification comes at the cost of losing some information about the finer flow dynamics (Forterre & Pouliquen 2003). More rigorously derived models, though mathematically more complex, have been proposed particularly to better characterize the stability conditions of sheet flows. For example, focusing on the power-law model and applying the weighted-residual technique (Ruyer-Quil & Manneville 1998, 2000), Amaouche, Djema & Bourdache (2009) and Fernandez-Nieto, Noble & Vila (2010) corrected the averaged momentum equation originally derived by Ng & Mei (1994) and formulated two-equation models consistent up to first order in the shallow-water parameter. Second-order models have been developed by Ruyer-Quil *et al.* (2012) and Noble & Vila (2013). A comprehensive overview of existing models incorporating yield stress, such as those for Herschel–Bulkley fluids, can be found in Denisenko (2024) and Muchiri, Monnier & Sellier (2025).

Governing equations (5.1)–(5.3), together with (5.4)–(5.5), are solved numerically using a standard cell-centred finite-volume method. The scheme is first-order accurate in both space and time. Details of the numerical implementation are provided in the Supplementary material.

The experimental tests described in § 4 have been numerically reproduced using a simplified square computational domain. This domain extends from the first measurement point upstream of the jump to the second measurement point downstream, resulting in a length of $L_x = 0.16$ m in the x-direction. The channel deviation begins at $x_d = 0.034$ m. A schematic representation of the computational domain for a deviation angle of $\theta = 15°$ is reported in the Supplementary material.

The bed channel slope values are set as follows: $S_{0x} = 0.06$, $S_{0y} = 0$ for both shear-thinning and Newtonian fluids; and $S_{0x} = 0.26$, $S_{0y} = 0$ for shear-thickening fluids.

The boundary conditions were designed to replicate the experimental set-up. At the left boundary of the computational domain, $x = 0$, the supercritical inflow conditions measured, namely the flow depth Y_0 and the flow rate per unit width $q_x = q_0 = Q/b$, were uniformly prescribed for all y. Consequently, the Froude number Fr_1, as reported in table 1, is imposed along the inflow boundary for all y.

An impermeability condition was applied along the sidewall and the wedge-shaped boundary corresponding to the channel deviation. At the right-hand and top boundaries, no explicit boundary conditions were enforced, assuming the flow remains supercritical as in the experiments in table 1. Therefore, only experimental cases that fulfilled this assumption were simulated.

The number of triangular cells varies with the deviation angle, ranging between 62 783 and 72 788. The time step was fixed at 10^{-4} s, which satisfies the Courant–Friedrichs–Lewy stability condition. To assess the quality of the numerical results, preliminary simulations neglecting the source terms were performed for all tests, and the numerical outcomes were compared with the theoretical predictions. The maximum relative differences were found to be 0.9 % and 0.6 % for β and η, respectively. When including the source terms, computations with a doubled mesh resolution demonstrated that the numerical results are mesh-independent.

5.2. *Two-dimensional simulation of selected experimental tests*

In this section, we analyse the numerical predictions of the shallow-water model formulated in (5.1)–(5.3), which incorporates bed friction and channel slope – factors present in the experiments but neglected in the simplified 1-D analytical model.

Detailed findings are presented for representative tests from table 1, one for each fluid rheology: shear-thinning, Newtonian and shear-thickening.

The results are presented in dimensionless form using the gate opening height h_G as reference length and $u_R = \sqrt{g h_G}$ as velocity scale, with $h_G = 5$ mm for the shear-thinning and Newtonian cases and $h_G = 3$ mm for the shear-thickening fluid. Dimensionless quantities are denoted with a superscript hat.

Figures 10(*a*), 10(*b*) and 10(*c*) show, in a colour map, the ratio F_* of the local Froude number to its critical value with streamlines superimposed for Test 4 ($n = 0.39$, $Fr_1 = 4.04$), Test 26 ($n = 1.00$, $Fr_1 = 4.21$) and Test 30 ($n = 1.09$, $Fr_1 = 5.14$) in table 1, respectively. For comparison, figure 10(*a–c*) include the straight shock front with slope β_{th} (see table 1) predicted by the 1-D model, shown as $\hat{y}_F^{1-\mathrm{D}}$ (black straight dashed line).

Regardless of the power-law exponent and consistent with the theoretical and experimental findings, figure 10(*a–c*) show that an oblique shock develops in all tests. Moreover, the flow remains supercritical ($F_* > 1$) downstream of the jump, i.e. a weak shock takes place.

However, the numerical shock front exhibits a slight concavity, with a local slope consistently greater than β_{th} for all $x \geqslant x_d$. Moreover, the streamline pattern downstream of the shock front indicates that the flow becomes approximately parallel to the deviated sidewall, particularly in the case of the shear-thinning fluid. A similar behaviour was reported by Gray & Cui (2007), who numerically investigated weak oblique shocks in granular flows on the free-surface generated by an abrupt channel deviation. Gray & Cui (2007) attributed the deformation of the shock front to the bottom friction and the slope of the channel, which determine the development of a gradually varied flow-depth profile along the channel and, consequently, the spatial variability of the Froude number

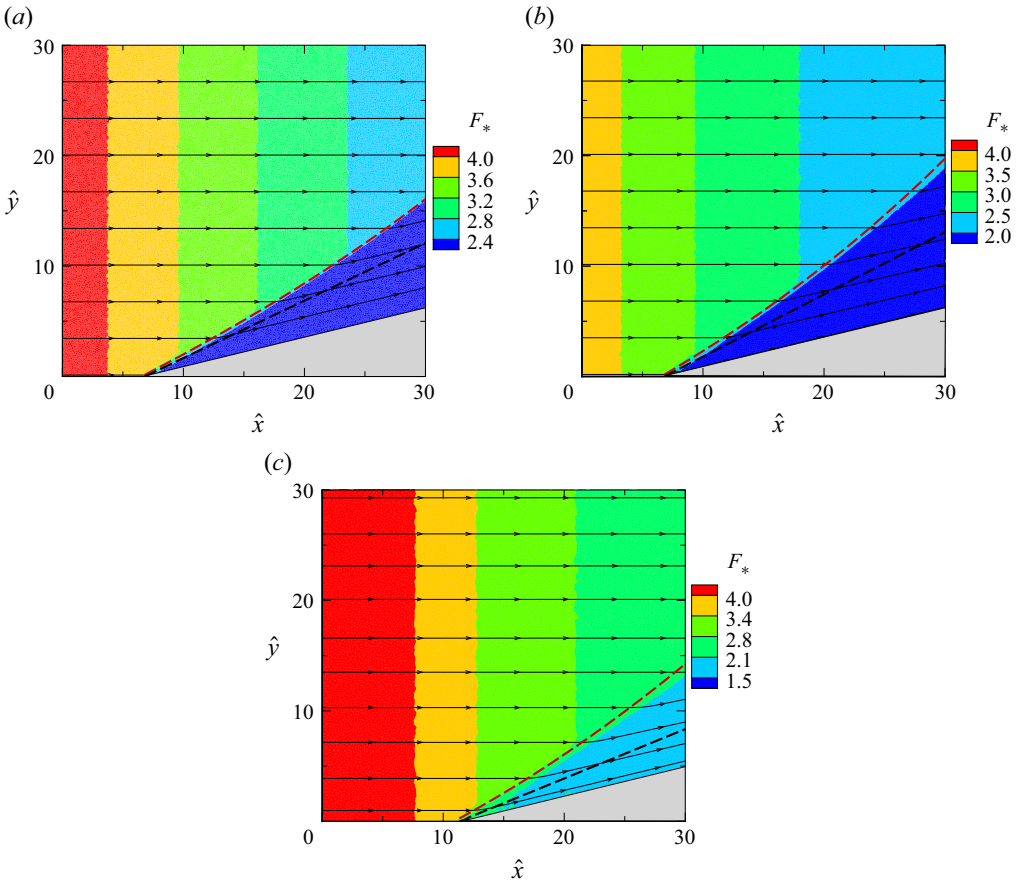

Figure 10. Contour plots of the $F_* = Fr/Fr_c$ ratio with streamlines superimposed. Black dashed line, shock front $\hat{y}_F^{1-\mathrm{D}}$; red dashed line, shock front $\hat{y}_F^{1-\mathrm{D}-S}$. (*a*) Test 4: shear-thinning fluid ($Fr_1 = 4.04$); (*b*) Test 26: Newtonian fluid ($Fr_1 = 3.48$); (*c*) Test 30: shear-thickening fluid ($Fr_1 = 5.14$).

upstream of the shock. This variability in the incoming Froude number along the shock front modifies the local Mach angle at the deviation edge, causing the shock to bend.

Figure 10(*a–c*) show that, as in granular flows, the Froude number Fr decreases markedly in the streamwise (x) direction upstream of the shock, indicating that a profile of depth of flow decelerated in the x direction occurs. In contrast, Fr remains essentially uniform in the transverse direction (y), as a consequence of the boundary conditions imposed at $x = 0$ (constant inflow) and at the sidewall $y = 0$ (impermeable boundary).

5.3. *One-dimensional model with source terms and comparison with the 2-D model*

This section introduces a 1-D model, derived from the 2-D formulation, which accounts for the influence of bed slope and friction. The analysis begins with an investigation of the mechanisms responsible for the curvature of the shock line observed in figure 10(*a–c*) and in some experimental tests. Following the approach of Gray & Cui (2007), it is assumed that the flow downstream of the shock remains aligned with the deviated sidewall. Furthermore, the source-term contributions (bed slope and friction) to the tangential and normal momentum equations across the shock are neglected. Under these assumptions, condition (3.8) is applied locally along the curved shock front $y_F = y_F(x)$.

Conversely, when the Froude number is defined approaching the shock front, the contributions of the source terms are retained. In other words, the present 1-D formulation partially accounts for the effects of bed slope and friction. The resulting problem to be solved can thus be written as

$$\frac{\mathrm{d}y_F}{\mathrm{d}x} = \tan\beta(x), \tag{5.6}$$

with the local Mach angle $\beta(x)$ satisfying the following algebraic equation adapted from (3.8):

$$\tan\theta = \frac{\tan(\beta\,(x))\left(3-\sqrt{1+8Fr_u^2\,C_M\sin^2(\beta\,(x))}\right)}{1-2\tan^2(\beta\,(x))-\sqrt{1+8Fr_u^2\,C_M\sin^2(\beta\,(x))}}, \tag{5.7}$$

where $Fr_u = Fr(x,\,y_F)$ denotes the Froude number upstream of the shock at the point with coordinates $(x,\,y_F)$.

Being independent of the inflow boundary condition y, the variation of the upstream Froude number in the x direction is obtained by integrating the steady 1-D counterpart (along x) of system (5.1)–(5.5), which can be expressed solely in terms of flow depth as follows:

$$\frac{\mathrm{d}Y}{\mathrm{d}x} = \frac{S_{0x}}{Y^{2n-2}}\frac{Y^{2n+1}-Y_N^{2n+1}}{Y^3-C_M Fr_N^2 Y_N^3}, \tag{5.8}$$

with the initial condition

$$Y\,(x=0) = Y_0. \tag{5.9}$$

In (5.8), Y_N denotes the normal, i.e. uniform, flow depth,

$$Y_N = \left[\frac{k}{\rho}\frac{1}{gS_{0x}}\left(\frac{2n+1}{n}q_0\right)^n\right]^{\frac{1}{2n+1}}, \tag{5.10}$$

and Fr_N is the normal Froude number, defined as $Fr_N = q_0/(gY_N^3)^{1/2}$.

Following the procedure suggested by Di Cristo, Iervolino & Vacca (2018), the analytical solution of the nonlinear ordinary differential (5.8), subject to the initial condition (5.9), has been derived (see Appendix B) and is given by

(for $n \neq 1/2$)

$$\begin{aligned} x = -\frac{Y_N}{S_{0x}}\Bigg[&\frac{1}{2n+2}\left(\frac{Y}{Y_N}\right)^{2n+2}\mathcal{F}\left(\frac{2n+2}{2n+1},\,1;\,\frac{4n+3}{2n+1};\left(\frac{Y}{Y_N}\right)^{2n+1}\right)\\ &-C_M Fr_N^{2\frac{1}{2n-1}}\left(\frac{Y}{Y_N}\right)^{2n-1}\mathcal{F}\left(\frac{2n-1}{2n+1},\,1;\,\frac{4n}{2n+1};\left(\frac{Y}{Y_N}\right)^{2n+1}\right)\\ &-\frac{1}{2n+2}\left(\frac{Y_0}{Y_N}\right)^{2n+2}\mathcal{F}\left(\frac{2n+2}{2n+1},\,1;\,\frac{4n+3}{2n+1};\left(\frac{Y_0}{Y_N}\right)^{2n+1}\right)\\ &+C_M Fr_N^{2\frac{1}{2n-1}}\left(\frac{Y_0}{Y_N}\right)^{2n-1}\mathcal{F}\left(\frac{2n-1}{2n+1},\,1;\,\frac{4n}{2n+1};\left(\frac{Y_0}{Y_N}\right)^{2n+1}\right)\Bigg]; \end{aligned} \tag{5.11}$$

(for $n = 1/2$)

$$x = \frac{Y_N}{S_{0x}}\left[\frac{Y}{Y_N} + \frac{1}{2}\ln\frac{Y - Y_N}{Y + Y_N} - \frac{C_M Fr_N^2}{2}\ln\frac{Y^2 - Y_N^2}{Y^2} - \frac{Y_0}{Y_N} - \frac{1}{2}\ln\frac{Y_0 - Y_N}{Y_0 + Y_N} + \frac{C_M Fr_N^2}{2}\ln\frac{Y_0^2 - Y_N^2}{Y_0^2}\right]. \tag{5.12}$$

In (5.11), $\mathcal{F}(a, b; c; z)$ denotes the Gauss hypergeometric function, often indicated as ${}_2F_1(a, b; c; z)$.

The numerical solution of system (5.6)–(5.7) is obtained via a standard explicit fourth-order Runge–Kutta scheme, initiated at the point $(x_d, 0)$. At each $x \geqslant x_d$ and at every Runge–Kutta stage, the flow depth upstream of the shock front $Y_u = Y(x, y_F)$ is determined iteratively by solving (5.11) (or (5.12) when $n = 1/2$). Consequently, the local Froude number is evaluated as $Fr_u = q_0/(gY_u^3)^{1/2}$. The local Mach angle $\beta(x)$ is then computed by iteratively solving (5.7).

The shock front computed with the 1-D formulation, which incorporates the source terms, is shown in figure 10(*a–c*) (denoted by $\hat{y}_F^{1-\mathrm{D}-S}$, red dashed line). The close agreement between the shock front locations predicted by the 1-D and 2-D models, as observed in figures 10(*a*) and 10(*b*), suggests that the local deceleration of the flow upstream of the front is the primary cause of the reduction of the Mach angle at the deviation edge and of the resultant curvature of the shock front. In contrast, figure 10(*c*) reveals a somewhat poorer correspondence between the predictions of the 2-D and 1-D models. Taking into account the relatively larger bottom slope in this test (15°), compared with the others (3.4°), the observed discrepancy is attributed to this significant slope. Specifically, the bottom slope determines a non-negligible weight component in the momentum balance across the shock and additionally reduces the flow parallelism with the deviated sidewall downstream of the shock.

Table 3 reports the value of the Froude number computed at the edge of the deviation Fr_d, obtained from (5.11), together with the inlet Froude number (Fr_1). In all cases, table 3 clearly shows a reduction in the Froude number at the edge of the deviation compared with the inlet value, the effect being particularly pronounced in tests involving shear-thickening fluids.

The reduced value of the Froude number at the deviation edge may lead to the formation of a detached shock. This phenomenon was observed in Tests 34–36 and 40–42, all involving shear-thickening fluids.

As a representative example of this condition, figure 11(*a*) depicts the colour map of the ratio F_* with superimposed streamlines for Test 42 ($n = 1.11$, $Fr_1 = 2.50$). Figure 11(*a*) clearly illustrates that the shock is detached and curved. For this case, the maximum deviation angle, calculated from (3.11) and (3.10) using the Froude number value $Fr_d = 1.40$ (see table 3), is $\theta_{max} \sim 11°$. Since the deviation angle in this test ($\theta = 25°$) exceeds θ_{max} the shock must detach. At the detachment point, the shock is normal, i.e. $\beta = 90°$. Moreover, as in the case of detached oblique-shock waves in gas dynamics (see, e.g. Anderson 2019), figure 11(*a*) shows that subcritical conditions ($F_* < 1$) occur immediately downstream of the shock (strong shock). Farther downstream, however, supercritical conditions are re-established ($F_* > 1$), indicating that the shock is weak.

To investigate in depth the magnitude of the shock front curvature, the transversal coordinate of the front at the abscissa of the downstream measurement point (x_M) predicted by the 2-D model ($y_{F,x_M}^{2-\mathrm{D}-S}$) is compared with the corresponding predictions

Test	Fr_1	Fr_d	Test	Fr_1	Fr_d
1	6.50	6.06	24	4.92	4.36
2	5.71	5.25	25	4.21	3.57
3	5.07	4.57	26	3.48	2.90
4	4.04	3.57	27	2.59	2.14
8	6.30	6.08	28	5.23	4.33
9	5.36	5.12	29	4.51	3.76
10	4.92	4.64	30	5.14	3.19
11	3.98	3.65	31	4.72	2.83
12	9.15	8.52	32	4.05	2.35
13	8.97	8.29	33	3.38	1.90
14	7.69	6.98	34	2.83	1.56
15	6.11	5.39	35	2.31	1.36
16	4.50	3.84	36	1.94	1.22
17	6.88	6.68	37	5.18	3.12
18	6.02	5.81	38	4.83	3.03
19	5.12	4.90	39	4.25	2.34
20	4.97	4.68	40	3.60	1.92
21	3.89	3.58	41	3.01	1.63
22	6.29	5.70	42	2.50	1.40
23	5.63	4.92			

Table 3. Inlet Froude number Fr_1 and Froude number Fr_d at the deviation edge x_d, for all simulated tests.

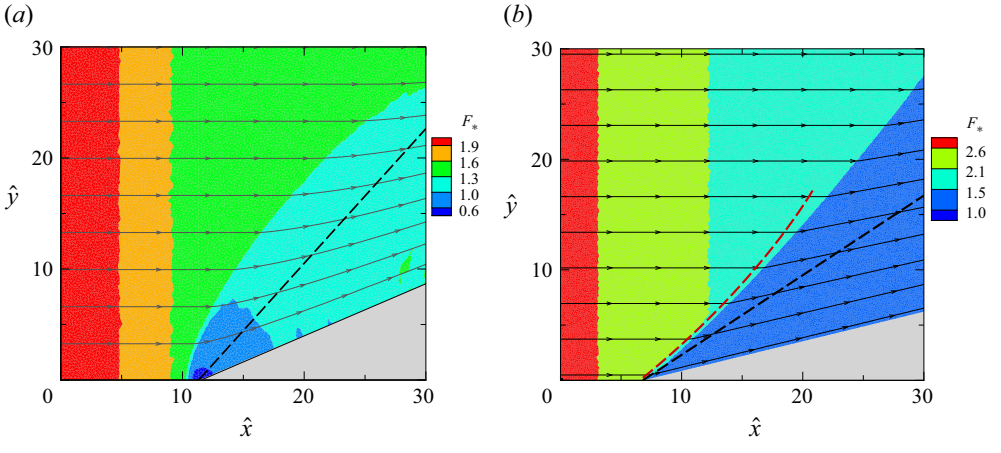

Figure 11. Contour plots of the $F_* = Fr/Fr_c$ ratio with streamlines superimposed. Black dashed line, shock front $\hat{y}_F^{1-\mathrm{D}}$; red dashed line, shock front $\hat{y}_F^{1-\mathrm{D}-S}$. (*a*) Test 42, shear-thickening fluid ($Fr_1 = 2.50$); (*b*) Test 27, Newtonian fluid ($Fr_1 = 2.59$).

of the 1-D formulations, both with ($y_{F,x_M}^{1-\mathrm{D}-S}$) and without ($y_{F,x_M}^{1-\mathrm{D}}$) source terms. Tests exhibiting detached shock have been excluded from this comparison. Table 4 reports, in dimensionless form, the computed values of $y_{F,x_M}^{2-\mathrm{D}-S}$, $y_{F,x_M}^{1-\mathrm{D}-S}$ and $y_{F,x_M}^{1-\mathrm{D}}$, together with the estimated uncertainty in determining $y_{F,x_M}^{2-\mathrm{D}-S}$.

Tests 21, 27 and 32–39 are not included in table 4, since, as in the cases with a detached shock, the reduction of Fr_u along the shock front becomes so pronounced that (5.7) no longer admits a solution. Consequently, the integration of (5.6)–(5.7) cannot be continued.

Test	n	θ	$\hat{y}^{2-D-S}_{F,x_M}$	$\hat{y}^{1-D-S}_{F,x_M}$	$\hat{y}^{1-D}_{F,x_M}$	Test	n	θ	$\hat{y}^{2-D-S}_{F,x_M}$	$\hat{y}^{1-D-S}_{F,x_M}$	$\hat{y}^{1-D}_{F,x_M}$
1	0.39	15	11.25 (3.7 %)	11.28	10.17	17	0.37	34	19.56 (2.2 %)	20.05	19.09
2	0.39	15	12.03 (3.9 %)	12.31	10.78	18	0.37	34	21.00 (2.9 %)	21.34	20.05
3	0.39	15	13.50 (4.0 %)	13.72	11.41	19	0.37	34	22.70 (2.3 %)	23.64	21.57
4	0.39	15	17.13 (2.4 %)	17.41	12.97	20	0.37	34	23.90 (2.1 %)	24.85	21.95
8	0.37	24	13.75 (3.7 %)	13.95	13.20	22	1.00	15	11.44 (4.2 %)	11.64	10.17
9	0.37	24	14.82 (3.1 %)	15.07	14.03	23	1.00	15	12.92 (4.0 %)	13.02	10.68
10	0.37	24	18.47 (4.2 %)	18.78	14.57	24	1.00	15	13.50 (5.0 %)	13.88	11.44
11	0.37	24	18.79 (2.2 %)	19.74	16.39	25	1.00	15	16.47 (3.0 %)	17.06	12.42
12	0.39	25	13.16 (3.5 %)	13.21	12.34	26	1.00	15	20.30 (2.5 %)	21.70	14.04
13	0.39	25	13.23 (3.4 %)	13.37	12.39	28	1.00	25	18.72 (3.0 %)	18.21	14.57
14	0.39	25	14.16 (3.1 %)	14.12	12.89	29	1.00	25	20.48 (2.7 %)	21.80	15.59
15	0.39	25	16.12 (2.2 %)	16.36	13.87	30	1.09	15	30.95 (3.1 %)	38.55	18.57
16	0.39	25	20.54 (3.2 %)	22.36	15.86	31	1.09	15	33.56 (3.2 %)	45.29	19.36

Table 4. Depth of the current at downstream measurement point x_M: results from 2-D model ($\hat{y}^{2-D-S}_{F,x_M}$) and from the 1-D formulation including ($\hat{y}^{1-D-S}_{F,x_M}$) and neglecting ($\hat{y}^{1-D}_{F,x_M}$) the source terms.

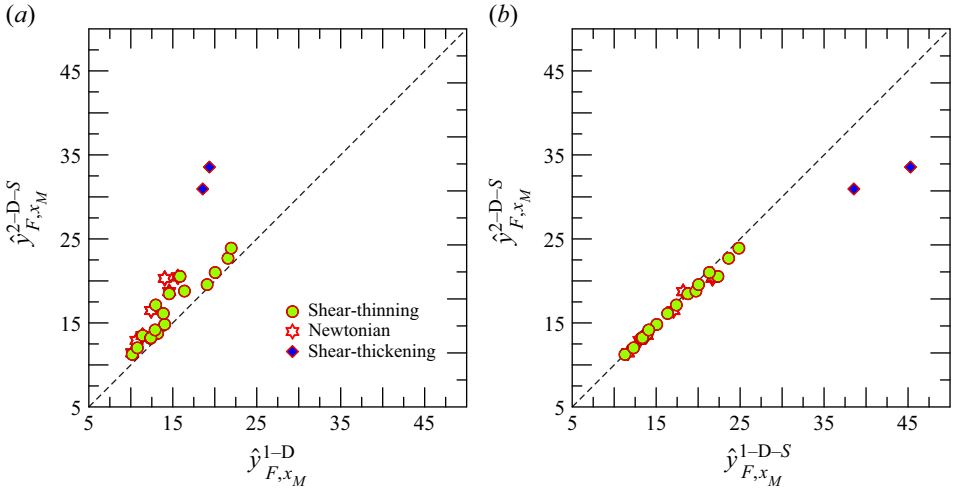

Figure 12. Depth of the current at downstream measurement point x_M predicted by the 2-D model, $\hat{y}^{2-D-S}_{F,x_M}$, compared with the results of the 1-D formulation (*a*) without the source terms, $\hat{y}^{1-D}_{F,x_M}$, and (*b*) including the source terms, $\hat{y}^{1-D-S}_{F,x_M}$.

As an illustration of these conditions, figure 11(*b*) shows the colour map of the ratio F_*, together with the streamlines for Test 27 ($n = 1.0$, $Fr_1 = 2.59$). Superimposed on the colour map are the shock fronts predicted by the 1-D formulation with source terms (red dashed line) and without source terms (black dashed line). Figure 11(*b*) highlights that the 1-D model with source terms reproduces the position of the shock front with reasonable accuracy only up to $\hat{x}^* = 21.5$; for $\hat{x} > \hat{x}^*$, it does not capture the correct shock position.

To aid readability and interpretation of table 4, figure 12 compares the dimensionless transverse coordinates of the shock front from the 2-D model, $\hat{y}^{2-D-S}_{F,x_M}$, with those predicted by the 1-D model without source terms, $\hat{y}^{1-D}_{F,x_M}$ (figure 12*a*) and with source terms $\hat{y}^{1-D-S}_{F,x_M}$ (figure 12*b*).

Figure 12 shows that for all tests with shear-thinning and Newtonian fluids (bed slope 3.4°) the reduction of the Froude number upstream of the shock, due to the bed slope and bottom friction, explains the difference observed between the predictions of the 1-D and 2-D models. This conclusion does not hold for tests 30 and 31 (shear-thickening fluid, bed slope 15°) in which the gravity-related source term plays a non-negligible role in the momentum balance and in determining the flow direction downstream the shock.

5.4. *Effect of bottom stress in the 2-D shallow-water model*

A careful inspection of the results of the 2-D shallow-water model shows that including shear stress leads to a concave deformation of the planar front predicted by the corresponding inviscid solution. This behaviour can be explained by noting that with increasing distance from the deflected sidewall, the length of the decelerated upstream flow profiles grows, causing a local reduction in the Froude number upstream of the jump. As illustrated in figure 3, a decrease in the upstream Froude number results in an increase of the Mach angle along the hypercritical branch of the curve. Consequently, the shock front shifts slightly farther away from the sidewall, in qualitative agreement with the larger Mach angles observed in some of the experiments (see figure 7).

6. Three-dimensional model

Previous 1-D analysis shows that the reduction in F_* upstream of the front due to the bottom resistance determines a concave Mach front. This result is essentially confirmed by the 2-D shallow-water modelling. However, both 1-D and 2-D shallow-water models are limited by several assumptions, mainly concerning the hydrostatic pressure distribution, the free-slip sidewall condition and the lack of representation of secondary flows. To assess the role of these assumptions, three-dimensional (3-D) flow features were examined through numerical simulations of selected experiments using the Open FOAM computational fluid dynamics (CFD) package, allowing a direct comparison with shallow-water predictions. The governing equations were solved using interFoam with a shear-dependent, power-law viscosity; the liquid–air interface was captured using a volume-of-fluid (VOF) method. Details of the numerical solver are provided in the Supplementary material.

A special inlet boundary condition was prescribed, specifying the customized inlet condition with both the fluid fraction for the VOF method and the velocity profile given by (2.2), with flow depth and discharge equal to those determined experimentally at the upstream sluice gate. A no-slip condition was imposed on all the solid boundaries, while a standard inlet–outlet condition was applied at the downstream end of the channel. The computational domain, which matches the geometry of the experimental channel, was discretized with refined hexahedral elements near the bottom and sidewalls. The domain was divided into 100×100 cells in the x and y directions and 60 cells in the z direction, for a total of 491 940 cells. Mesh sensitivity was preliminarily assessed by repeating the simulation on a finer mesh obtained by increasing the number of cells along each direction by a factor of 1.5. Changes of the flow depth and of the depth-averaged velocity magnitude at the downstream measuring point, Y_2 and V_2, respectively, were used to assess the dependence of the computed flow variables on the discretization. Variations in the computed values of Y_2 and V_2 were found to be approximately 1 %, therefore providing acceptable confidence in the results calculated with the coarser resolution, which has been used for the remaining of the analysis. The interested reader is referred to the Supplementary material for a further assessment of the mesh sensitivity of the computed flow field.

For a more straightforward comparison with shallow-water models, the depth-averaged flow properties have been extracted from the computed 3-D flow field. Namely, the flow depth and the depth-averaged velocity components were computed as

$$\mathcal{Y} = \int_0^H \varphi \mathrm{d}z, \tag{6.1}$$

$$\mathcal{V}_x = \frac{1}{\mathcal{Y}} \int_0^H \varphi u_x \mathrm{d}z, \tag{6.2}$$

$$\mathcal{V}_y = \frac{1}{\mathcal{Y}} \int_0^H \varphi u_y \mathrm{d}z, \tag{6.3}$$

in which H denotes the height of the computational domain, φ is the volume fraction of water, u_x, u_y are the Cartesian velocity components along the x and y axes, respectively.

The corresponding depth-integrated Froude number has been evaluated as

$$\mathcal{F}r = \frac{|\boldsymbol{\mathcal{V}}|}{\sqrt{g\mathcal{Y}}}. \tag{6.4}$$

Finally, the following dimensionless parameter Ψ has been introduced to measure the effects of vertical inertia in terms of deviations from the hydrostatic pressure distribution:

$$\Psi = \sqrt{\frac{1}{\mathcal{Y}} \int_0^H \varphi \left[\frac{p(z) - p_h(z)}{p_{h,b}} \right]^2 \mathrm{d}z}. \tag{6.5}$$

In (6.5), $p_h(z)$ and $p_{h,b}$ denote the hydrostatic pressure value at elevation z and at the bottom, respectively.

The sample results of the numerical simulations are shown, in dimensionless coordinates and variables, in figures 13 (Test 4, shear-thinning fluid) and 14 (Test 30, shear-thickening fluid). Both figures 13(*a*) and 14(*a*) show the isolines of the Ψ parameter superposed to the colour map of $\hat{z}_{fs}$, representing the dimensionless elevation of the $\varphi = 0.1$ surface. In the figure the front positions of the 1-D model with ($\hat{y}_F^{1-\mathrm{D}-S}$, red dashed-line) or without ($\hat{y}_F^{1-\mathrm{D}}$, white dashed-line) the source terms are also depicted. Figures 13(*b*) and 14(*b*) show the isolines of $F_* = \mathcal{F}r/Fr_c$ superposed to the same colour map, along with the streamlines of the reconstructed depth-averaged flow field $\mathcal{V}$. Finally, figures 13(*c*) and 14(*c*) represent the dimensionless pressure field in the normal-to-the-sidewall direction, $\hat{\xi}$, on three slices at increasing distance along the deviated sidewall, namely $\hat{x} = 15$, 22.5 and 30. The same figures also report the vorticity lines deduced from the computed flow field.

Preliminarily we observe that the VOF does not provide an explicit representation of the free-surface, differently from the interface-capturing level-set method (Osher & Fedkiw 2001) or the surface-fitting method (Ramaswamy & Kawahara 1987). Indeed, the absence of a clear indication of a discontinuous free surface hinders the possibility to define the shock front unambiguously. However, the representation of the free surface through the $\varphi = 0.1$ value provides reasonable agreement with the shock location predicted by the depth-averaged models (figures 13*a* and 14*a*) confirming the concavity of the front especially for the shear-thinning case, and it is therefore considered in what follows.

Figure 13(*a*) shows that the Ψ parameter is $O(10^{-3})$ for Test 4, while in Test 30 it is $O(10^{-2})$ (figure 14*a*). Therefore, the shallow-water assumption of hydrostatic pressure distribution is largely fulfilled for the shear-thinning case, and still acceptable also for the shear-thickening one. This observation is further confirmed by the reconstructed depth-averaged streamlines, which closely resemble those computed in the 2-D shallow-water

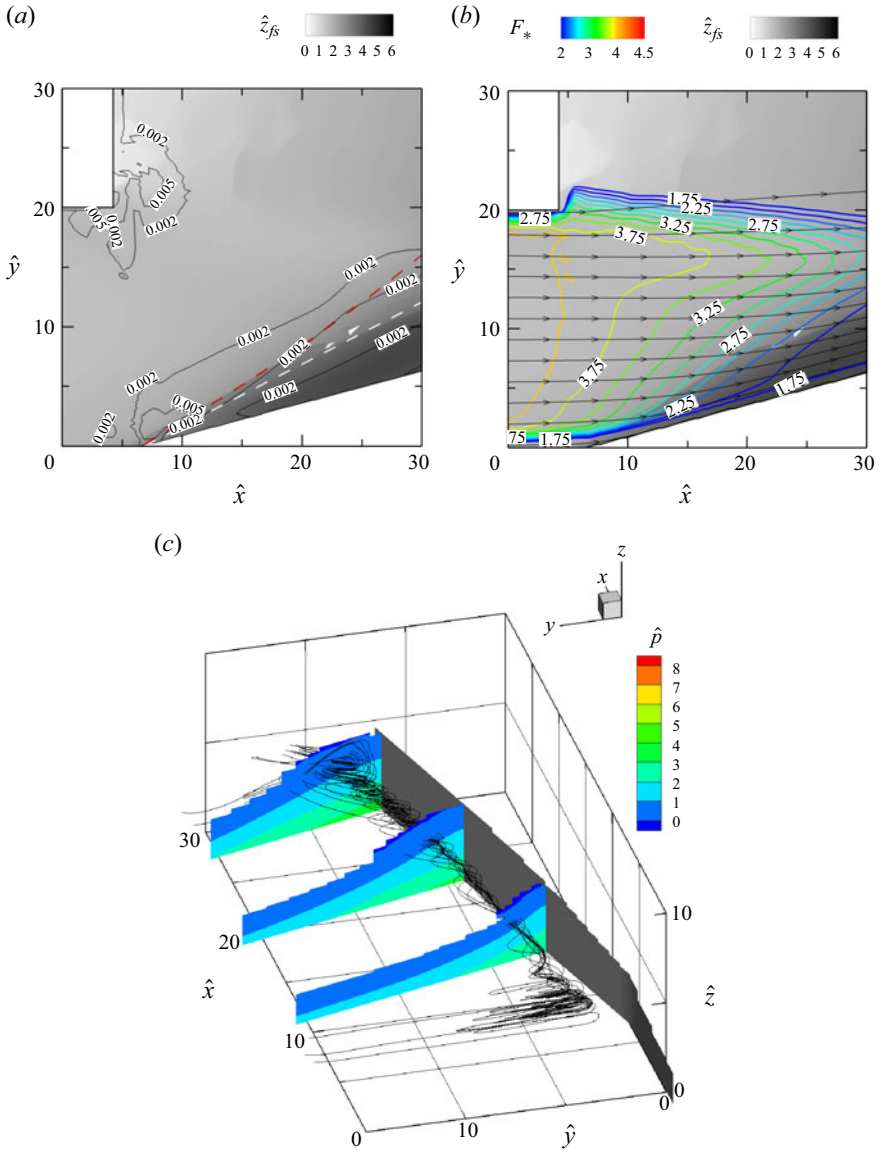

Figure 13. Test 4, shear-thinning fluid. (*a*) Colour map of the dimensionless elevation of the $\varphi = 0.1$ surface with the isocontours of the Ψ parameter. White dashed-line, $\hat{y}_F^{1-\mathrm{D}}$; red dashed-line, $\hat{y}_F^{1-\mathrm{D}-S}$. (*b*) Colour map of the dimensionless elevation of the $\varphi = 0.1$ surface with streamlines of the depth-averaged flow field and isocontours of the F_* ratio. (*c*) Pressure distribution in three normal-to-the deviated sidewalls cross-sections. Vortex lines are also shown.

simulations (figures 10*a* and 10*c*), although their curvature is more gradual. Contour plot of dimensionless vertical velocity component reported in the Supplementary material confirms this conclusion.

In the shear-thinning case, figure 13(*c*) shows that the vorticity lines are predominantly aligned with the streamwise direction, while the transverse pressure gradient exhibits a marked variation along the deviated sidewall. In terms of global quantities, this is reflected in the pronounced upstream variation of F_* along the front, visible in figure 13(*b*). This

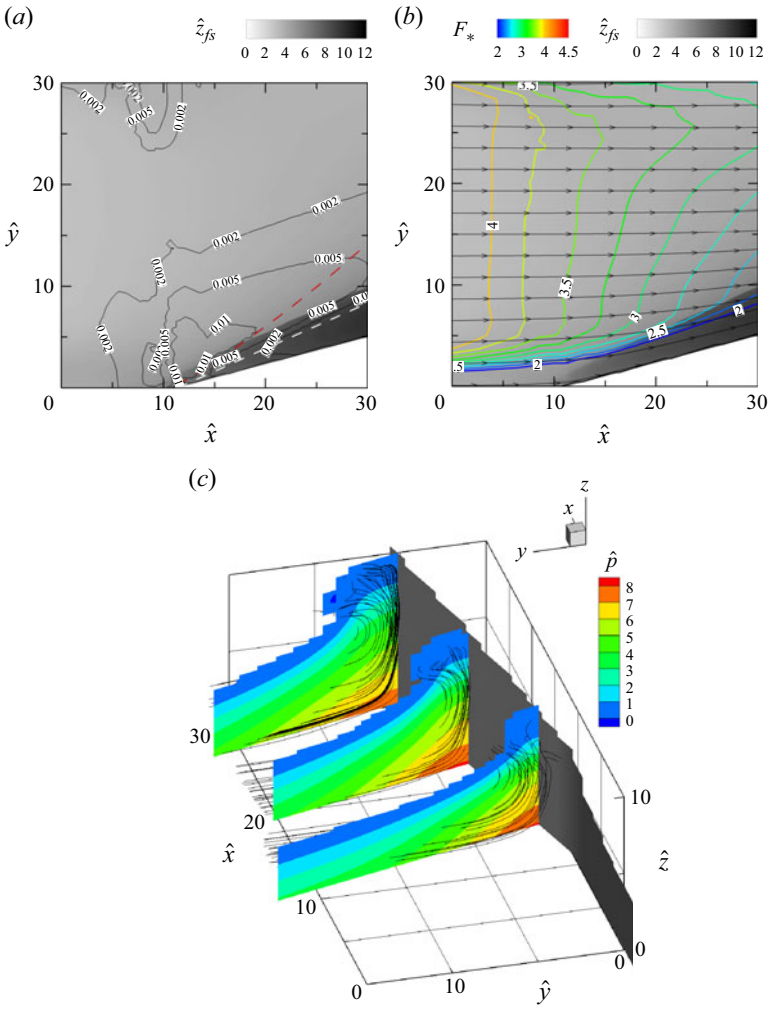

Figure 14. Test 30, shear-thickening fluid. See figure 13 for caption.

behaviour indicates an enhancement of the mixing between the near-wall region and the outer flow, which promotes a stronger penetration of the front into the core of the incoming flow. By contrast, in the shear-thickening case (figure 14*c*), the vorticity lines are essentially located on transverse planes and the transverse pressure gradient only varies weakly along the deviated sidewall. Consistently, the front displays a less pronounced concavity and approximately follows the $F_* = 2.25$ contour, see figure 14(*b*).

With regard to the role of lateral friction, the thickness of the boundary-layer developing from the deviated sidewall contributes in defining whether the front penetrates into the outer region and, consequently, if it is influenced by the streamwise decay of F_* occurring therein. The boundary-layer thickness depends explicitly on the power-law exponent n. Indeed, for a fixed value of the generalized Reynolds number based on the streamwise distance, Re_x, the boundary layer is expected to be thinner in a shear-thinning fluid than in a shear-thickening one (see, e.g. Kudenatti, Noor-E-Misbah & Bharathi 2021). In the case of shear-thinning fluid, see figure 13(*b*), the front penetrates into the outer region, experiencing a marked upstream variation of F_* along its length and showing a fair

agreement with the concave behaviour predicted by the 1-D formulation including source terms (1-D–S). Conversely, figure 14(*b*) shows that, in the shear-thickening case, where Re_x is comparable to the one of Test 4, the front is located closer to the deviated sidewall and approximately follows the $F_* = 2.25$ contour, resulting in a flatter shape than that predicted by the 1-D–S model. These results indirectly confirm the relevant role of the streamwise variation of the Froude number in driving the bending of the front, as predicted by the 1-D model.

Overall, the comparison between depth-averaged and depth-resolved flow fields suggests a closer agreement of the simplified model for the shear-thinning fluid case, compared with the shear-thickening one.

7. Discussion and conclusions

This study examines the formation and structure of oblique shocks – both weak and strong (hydraulic jumps) – in shallow laminar flows of power-law fluids past abrupt channel deviations, using a combination of analytical developments, laboratory experiments and numerical modelling in both the 2-D averaged depth formulations and the 3-D formulations. The work provides a unified description of these flows and clarifies the respective roles of non-Newtonian rheology, flow regime and channel geometry in shaping shock morphology. The findings are relevant to the environmental management of mine tailings, such as those presented by Burger *et al.* (2010*b*) for laminar flow, industrial wastes and slurries, debris and lava flows, and have further applications in the health and food industries, as well as in cooling, coating, cleaning and injection processes.

The first component of the study is the development of a simplified analytical framework extending classical oblique-jump theory to power-law fluids. By coupling the constitutive relation with the continuity and momentum balance equations in the two coordinate directions, under the assumption of a hydrostatic pressure distribution, we derive a system of three transcendental equations for three unknowns. For a specified rheology, the model predicts the onset conditions for oblique shocks and the Mach angle that governs the orientation of the shock front as a function of the upstream Froude number and the channel deflection angle. These predictions reduce to the inviscid solution in the limit of a Boussinesq coefficient equal to unity. Moreover, it has been shown that the inviscid solution to the problem for a power-law fluid coincides with that for turbulent clear water, provided that the Froude numbers are scaled by their critical value.

In a steady rapid current of a power-law fluid past an abrupt channel deflection, three flow responses are possible. For sufficiently large upstream Froude numbers and small deflection angles, there are two oblique shock solutions: a strong shock with a larger front angle, where the downstream flow becomes subcritical and a hydraulic jump develops, and a weak shock with a smaller angle, where the flow remains supercritical and the front simply connects two rapid-flow states. When the deflection angle exceeds a critical value θ_{max} or the upstream Froude number is too small, attached oblique shocks no longer exist and the shock front detaches from the corner and curves downstream.

Laboratory experiments in deflected channels documented the structure and evolution of oblique shocks over a wide range of rheologies, geometries, and flow conditions. To investigate rheological effects, three classes of working fluids were employed: (i) a shear-thinning mixture of water, glycerol and xanthan gum; (ii) a shear-thickening suspension of corn starch, formulated to prevent sedimentation and inhibit biodegradation; (iii) a viscous Newtonian water–glycerol mixture prepared to maintain laminar flow. These fluids covered a flow-behaviour index between 0.37 and 1.11. The channel deflection angles ranged from 15° to 34°. By adjusting the flow rate, the upstream Froude numbers Fr_1 between 1.72 and

9.15 were achieved, corresponding to the upstream Reynolds numbers Re_1 in the range 12–374.

The observations from high-resolution video recordings confirm that non-Newtonian flows develop oblique shocks and hydraulic jumps. At low Fr_1, the jump typically exhibited an undular form with two low crests downstream of the corner, whereas at high Fr_1 it developed into a well-defined wall jet.

All experimental input and output variables were subjected to an uncertainty analysis, which yielded global relative errors of 11 % for the dimensionless depth ratio η, 5 % for the Mach angle β and 21 % for the upstream Reynolds number Re_1. A comparison between the theoretical 1-D predictions and the experimental results showed generally good agreement, with the experimental error bars typically encompassing the theoretical curves. For the Mach angle β, the agreement is the closest for shear-thinning fluids, whereas shear-thickening and especially Newtonian fluids exhibit a systematic overprediction of β by theory. For the depth ratio η, the agreement is excellent at large Fr_1, less so at lower Fr_1 due to measurement issues. At very high Fr_1 values, the discrepancies become noticeable again due to the jet-shaped structure of the jump in the area in contact with the inclined wall, particularly near the corner. Note that the 3-D structure of the flow field is also visible in figures 13 and 14, showing the results of the depth-resolved model.

Numerical simulations were developed at two levels of complexity, using a proprietary code that implements shallow-water theory for depth-averaged (2-D) simulations and the Open FOAM CFD package for depth-resolved (3-D) simulations.

The shallow-water model incorporates bed friction and the experimental slope of the channel, absent in the 1-D analytical scheme. Representative simulations for shear-thinning, Newtonian and shear-thickening fluids confirm that oblique shocks form in nearly all cases, with the downstream flow remaining supercritical, indicative of weak shocks. Compared with the straight theoretical front, the numerically predicted shock front exhibits a slight concavity and a larger local slope. Streamline patterns downstream of the shock show flow alignment with the deviated sidewall, most pronounced for shear-thinning fluids. This deformation of the front, also reported in granular flows, is attributed to bed friction and channel slope, which produce a streamwise decrease of the upstream Froude number and thus a bending of the shock. The observed shock curvature was interpreted using a simplified 1-D formulation that applies the oblique-shock condition pointwise along the front, while partially accounting for bed slope and friction effects through the local Froude number upstream of the front. This approach captures the gradual bending of the shock induced by the friction of the bed and the slope of the channel. The shock front predicted by the 1-D model that includes source terms closely matches the 2-D numerical results in most cases, indicating that local flow deceleration upstream of the shock is the primary cause of the reduced Mach angle and shock curvature. However, in the case with a higher bottom slope (15°), the agreement deteriorates due to the significant impact of the slope on the momentum balance across the shock and the reduced flow alignment with the deviated sidewall downstream of the shock.

Shear-thickening fluids can lead to shock detachment when the channel deflection angle exceeds a critical value, as demonstrated in Test 43. In this case, the shock detaches at a normal angle, producing a strong subcritical region immediately downstream, followed farther downstream by a return to weak supercritical flow conditions. This behaviour is analogous to the detached oblique shocks observed in gas dynamics.

Three-dimensional flow characteristics were investigated using numerical simulations with the openFOAM CFD package, combining the interFoam solver, the VOF method and a shear-dependent viscosity. Simulated results show that shallow water hydrostatic pressure distribution assumption is largely fulfilled for shear-thinning and shear-thickening

fluids. For shear-thinning fluids the flow shows a concave deformation near the shock, consistent with 1-D model predictions, while the shear-thickening case exhibits less alignment with the deviated sidewall and differs from the 2-D depth-averaged flow. In general, the depth-resolved simulations match the predictions of the shallow-water model more closely for shear-thinning and Newtonian fluids than for shear-thickening ones.

In general, the 1-D model captures the front location with reasonable accuracy, while the 2-D model provides an improved description of front curvature and flow redistribution. The 3-D simulations offer the most comprehensive representation of the velocity field and wall effects, without being constrained by the hydrostatic pressure assumption. These results highlight the importance of selecting an appropriate level of model complexity according to the fluid rheology and flow configuration.

Future work should focus on extending these analyses to more complex flow conditions, including a broader spectrum of non-Newtonian rheologies, such as the Carreau–Yasuda model and models accounting for yield stress, like the Herschel–Bulkley fluid, using rigorously derived approaches (e.g. Muchiri *et al*. 2025). Additionally, investigations should consider irregular channel geometries, transition to turbulence and fully developed turbulence. In particular, the extension to more complex rheologies will significantly broaden the applicability of the theory, especially in environmental and industrial contexts.

High-resolution 3-D simulations could be used to investigate the influence of turbulence, secondary flows and free-surface instabilities, which are not fully captured by depth-averaged models. In parallel, experimental studies under controlled laboratory conditions would provide valuable datasets to refine the model calibration and validate predictions of shock curvature and detachment, also under strong shock conditions. Another promising direction lies in the development of hybrid modelling strategies in which simplified 1-D or 2-D formulations are dynamically coupled with local 3-D corrections, offering an effective compromise between computational efficiency and physical accuracy. Such efforts will help bridge the gap between idealized theoretical models and the complex dynamics observed in real-world flows.

Supplementary material. Supplementary material is available at https://doi.org/10.1017/jfm.2026.11509.

Acknowledgements. The authors thank Dr S. Hasheminejad for his support in the experiments.

Funding. S.L. acknowledges that this work was supported by a Project funded under the National Recovery and Resilience Plan (NRRP), Mission 4 Component 2 Investment 1.5 – Call for tender no. 3277 of 30/12/2021 of the Italian Ministry of University and Research funded by the European Union – NextGenerationEU. Project code ECS00000033, Concession Decree no. 1052 of 23/06/2022 adopted by the Italian Ministry of University and Research, CUP D93C22000460001, 'Ecosystem for Sustainable Transition in Emilia-Romagna' (Ecosister), Spoke 4. S.L. also acknowledges the funding from FIL Azione A, Bando 2021, University of Parma.

Declaration of interests. The authors report no conflict of interest. The numerical information provided in the figures is produced by solving the equations in the paper. The results of the experiments are available from the authors on request.

Appendix A

In this appendix, (3.1)–(3.3) are derived using an approach commonly employed in gas dynamics for the analysis of oblique shock waves (Anderson 2019).

Consider the flow over a horizontal plane while neglecting bottom friction. The hyperbolic nature of (5.1)–(5.3) implies that, under supercritical flow conditions, shock waves may develop, producing discontinuities in flow depth and velocity across a singular surface. To characterize these discontinuities, a limiting process is applied to derive the jump conditions for the mass and the momentum (both tangential and normal) across the

shock. In steady state, these conditions take the form (Marsden & Hughes 1994)

$$[[Y\boldsymbol{V}\cdot\boldsymbol{n}]]=0, \tag{A1}$$

$$\left[\left[C_M Y\boldsymbol{V}\,(\boldsymbol{V}\cdot\boldsymbol{n})+g\frac{Y^2}{2}\boldsymbol{n}\right]\right]=0, \tag{A2}$$

where $\boldsymbol{n}$ is the unit normal vector to the singular surface, and $[[\ldots]]$ denotes the jump of a quantity across the shock.

Specializing in the problem addressed here (see § 2), (A1)–(A2) can be expressed as

$$Y_1\,|\boldsymbol{V}_1|\sin\beta=Y_2\,|\boldsymbol{V}_2|\sin(\beta-\theta), \tag{A3}$$

$$C_M Y_1\,|\boldsymbol{V}_1|^2\sin\beta\cos\beta=C_M Y_2\,|\boldsymbol{V}_2|^2\sin(\beta-\theta)\cos(\beta-\theta), \tag{A4}$$

$$C_M Y_1\,|\boldsymbol{V}_1|^2\sin^2\beta+g\frac{Y_1^2}{2}=C_M Y_2\,|\boldsymbol{V}_2|^2\sin^2(\beta-\theta)+g\frac{Y_2^2}{2}. \tag{A5}$$

It can be easily verified that (A3)–(A5), expressed as dimensionless variables, lead to (3.4).

Appendix B

This appendix provides further details on the derivation of the analytical solution (5.11)–(5.12) for the separable ordinary differential equation (5.8). Introducing the non-dimensional flow depth $\phi=Y/Y_N$, separation of variables and subsequent integration of (5.8) yields

$$x+const=\frac{Y_N}{S_{0x}}\left[\int\frac{\phi^{2n+1}}{\phi^{2n+1}-1}\mathrm{d}\phi-C_M Fr_N^2\int\frac{\phi^{2n-2}}{\phi^{2n+1}-1}\mathrm{d}\phi\right]. \tag{B1}$$

By introducing the auxiliary variable $\psi=\phi^{\alpha}$, with $\alpha=1/(2n+1)$, the (B1) can be recast in the form

$$x+const=-\alpha\frac{Y_N}{S_{0x}}\left[\int\psi^{\alpha}(1-\psi)^{-1}\mathrm{d}\psi-C_M Fr_N^2\int\psi^{2\alpha}(1-\psi)^{-1}\mathrm{d}\psi\right]. \tag{B2}$$

Both integrals on the right-hand side of (B2) are evaluated using the Chebyshev integral identity (Weisstein 1998),

$$\int\psi^{p}\,(1-\psi)^{q}\,\mathrm{d}\psi=\frac{\psi^{1+p}}{1+p}\mathcal{F}\,(1+p,-q;2+p;\psi), \tag{B3}$$

where $\mathcal{F}(a,b;c;z)$ denotes the Gauss hypergeometric function. Consequently, the solution of (5.8) for the flow depth Y can be expressed as

$$\begin{aligned}x+const=-\frac{Y_N}{S_{0x}}\Bigg[&\frac{1}{2n+2}\left(\frac{Y}{Y_N}\right)^{2n+2}\mathcal{F}\left(\frac{2n+2}{2n+1},1;\frac{4n+3}{2n+1};\left(\frac{Y}{Y_N}\right)^{2n+1}\right)\\&-C_M Fr_N^2\frac{1}{2n-1}\left(\frac{Y}{Y_N}\right)^{2n-1}\mathcal{F}\left(\frac{2n-1}{2n+1},1;\frac{4n}{2n+1};\left(\frac{Y}{Y_N}\right)^{2n+1}\right)\Bigg].\end{aligned} \tag{B4}$$

It should be noted that (B4) becomes singular for $n=1/2$. In this special case, (B2) reduces to

$$x+const=-\frac{Y_N}{S_{0x}}\left[\int\frac{\sqrt{\psi}}{1-\psi}\,\mathrm{d}\psi-C_M Fr_N^2\int\frac{1}{\psi\,(1-\psi)}\mathrm{d}\,\psi\right], \tag{B5}$$

and therefore the solution of (5.8) is

$$x + const = \frac{Y_N}{S_{0x}} \left[\frac{Y}{Y_N} + \frac{1}{2} \ln \frac{Y - Y_n}{Y + Y_N} - \frac{C_M Fr_N^2}{2} \ln \frac{Y^2 - Y_N^2}{Y^2} \right]. \tag{B6}$$

Applying the initial condition (5.9), (5.11) and (5.12) are obtained directly.

References

Amaouche, M., Djema, A. & Bourdache, L. 2009 A modified Shkadov's model for thin film flow of a power law fluid over an inclined surface. *C. R. Méc.* **337** (1), 48–52.

Ancey, C. 2007 Plasticity and geophysical flows: a review. *J. Non-Newtonian Fluid Mech.* **142**, 4–35.

Anderson, J.D. 2019 *Hypersonic and High-Temperature Gas Dynamics*. American Institute of Aeronautics and Astronautics.

Bakhmeteff, B.A. 1932 *Hydraulics of Open Channels*. McGraw-Hill.

Beltrami, G.M., Repetto, R. & Del Guzzo, A. 2007 A simple method to regularize supercritical flow profiles in bends. *J. Hydraul. Res.* **45** (6), 773–786.

Borger, D.V. 2013 Rheology of slurries and environmental impacts in the mining industry. *Annu. Rev. Chem. Biomol. Engng* **4**, 239–256.

Burger, J., Haldenwang, R. & Alderman, N. 2010*a* Experimental database for non-Newtonian flow in four channel shapes. *J. Hydraul. Res.* **48**, 363–370.

Burger, J., Haldenwang, R. & Alderman, N. 2010*b* Friction factor-Reynolds number relationship for laminar flow of non-Newtonian fluids in open channels of different cross-sectional shapes. *Chem. Engng Sci.* **65**, 3549–3556.

Busemann, A. 1931 Gasdynamik. In *Handbuch der Experimentalphysik*, vol. 4. Wien-Harms.

Campomaggiore, F., Di Cristo, C., Iervolino, M. & Vacca, A. 2016 Development of roll-waves in power-law fluids with non-uniform initial conditions. *J. Hydraul. Res.* **54** (3), 289–306.

Carotenuto, C., Merola, M.C., Álvarez-Romero, M., Coppola, E. & Minale, M. 2015 Rheology of natural slurries involved in a rapid mudflow with different soil organic carbon content. *Colloids Surf. A: Physicochemical Engng Aspects* **466**, 57–65.

Causon, D.M., Mingham, C.G. & Ingram, D.M. 1999 Advances in calculation methods for supercritical flow in spillway channels. *J. Hydraul. Engng* **125** (10), 1039–1050.

Chanson, H. 2009 Current knowledge in hydraulic jumps and related phenomena. A survey of experimental results. *Eur. J. Mech. B-Fluids* **28** (2), 191–210.

Chiappini, D. 2020 A lattice-Boltzmann free surface model for injection moulding of a non-Newtonian fluid. *Phil. Trans. A Math. Phys. Engng Sci.* **378** (2175), 20190407.

Chimetta, B.P. & Franklin, E.M. 2023 A robust numerical strategy for finding surface waves in flows of non-Newtonian liquids. *J. Non-Newtonian Fluid Mech.* **322**, 105153.

Chow, V.T. 1959 *Open-Channels Hydraulics*. McGraw-Hill.

Citrini, D. 1940 Sul movimento di una corrente veloce in un canale in curva. *L'Energia Elettrica* **17**, 509–525.

Citrini, D. 1950 Recensione su correnti veloci nei canali aperti. *L'Energia Elettrica* **27**, 581–586.

Cui, X., Gray, J.M.N.T. & Johannesson, T. 2007 Deflecting dams and the formation of oblique shocks in snow avalanches at Flateyri, Iceland. *J. Geophys. Res.* **112**, F04012.

Dallagi, H., Faille, C., Bouvier, L., Deleplace, M., Dubois, T., Aloui, F. & Benezech, T. 2022 Wet foam flow: a suitable method for improving surface hygiene in the food industry. *J. Food Engng* **322**, 110976.

Darby, R. 1986 Laminar and turbulent pipe flows of non-Newtonian fluids. In *Encyclopedia of Fluid Mechanics* (ed. N.P. Cheremisinoff), Rheology and Non-Newtonian Flows, vol. 7, pp. 19–53. Gulf Publishing Co.

Denisenko, D. 2024 *Modelling Free-surface Flows of Yield-stress Fluids, Application to the Simulation of Natural Hazards*. Université Grenoble Alpes. NNT: 2024GRALI108. Tel-051140398.

De Padova, D. & Mossa, M. 2021 Hydraulic jump: a brief history and research challenges. *Water* **13**, 1733.

Di Cristo, C., Iervolino, M. & Vacca, A. 2018 Applicability of Kinematic and diffusive models for mud-flows: a steady state analysis. *J. Hydrol.* **559**, 585–595.

Di Federico, V. 1998 Permanent waves in slow free-surface flow of a Herschel–Bulkley fluid. *Meccanica* **33**, 127–137.

Engelund, F. & Munch-Petersen, J. 1953 Écoulement permanent dans les canaux convergents et divergents. *La Houille Blanche* **38**, 464–481.

FERNANDEZ-NIETO, E.D., NOBLE, P. & VILA, J.P. 2010 Long-surface wave instability in dense granular flows. *J. Non-Newtonian Fluid Mech.* **165**, 712–732.
FORTERRE, Y. & POULIQUEN, O. 2003 Long-surface wave instability in dense granular flows. *J. Fluid Mech.* **486**, 21–50.
GRAY, J.M.N.T. & CUI, X. 2007 Weak, strong and detached oblique shocks in gravity-driven granular free-surface flows. *J. Fluid Mech.* **579**, 113–136.
GRECO, M., DI CRISTO, C., IERVOLINO, M. & VACCA, A. 2019 Numerical simulation of mud-flows impacting structures. *J. Mountain Sci.* **16** (2), 364–382.
GUZEL, B., BURGHELEA, T., FRIGAARD, I.A. & MARTINEZ, D.M. 2009 Observation of laminar–turbulent transition of a yield stress fluid in Hagen–Poiseuille flow. *J. Fluid Mech.* **627**, 97–128.
HAGER, W.H., SCHWALT, M., JIMENEZ, O. & CHAUDHRY, H.M. 1994 Supercritical flow near an abrupt wall deflection. *J. Hydraul. Res.* **32** (1), 103–118.
HALDENWANG, R. & SLATTER, P. 2006 Experimental procedure and database for non-Newtonian open channel flow. *J. Hydraul. Res.* **44**, 283–287.
HOGG, A.J. & PRITCHARD, D. 2004 The effects of hydraulic resistance on dam-break and other shallow inertial flows. *J. Fluid Mech.* **501**, 179–212.
HORNER, J.S., WAGNER, N.J. & BERIS, A.N. 2021 A comparative study of blood rheology across species. *Soft Matt.* **17**, 4766.
IPPEN, A.T. 1936 An analytical and experimental study of high velocity flow in curved sections of open channels. PhD thesis, California Institute of Technology, CA, USA.
IPPEN, A.T. 1943 Gas-wave analogies in open-channel flow. In *Proceedings of the II Hydraulics Conference*, pp. 248–265. Iowa Institute of Hydraulic research, State University of Iowa.
IPPEN, A.T. & KNAPP, R.T. 1936 A study of high-velocity flow in curved channels of rectangular cross-section. *EOS Trans. AGU* **17**, 516–521.
KNAPP, R.T. & IPPEN, A.T. 1938 Curvilinear flow of liquids with free surfaces at velocities above that of wave propagation. In *Proceedings of the V International Congress of Applied Mechanics*, pp. 516–521. Cambridge University Press.
KOZIC, M.S., RISTIC, S.S., LINIC, S.L., HIL, T. & STETIC-KOZIC, S. 2016 Numerical analysis of rotational speed impact on mixing process in a horizontal twin-shaft paddle batch mixer with non-Newtonian fluid. *FME Transactions* **44** (2), 115–124.
LATKOVIC, D. & LEVY, E.K. 1991 The flow characteristics of fluidized magnetite powder in an inclined open channel. *Powder Technol.* **67** (2), 207–216.
KUDENATTI, R.B., NOOR-E-MISBAH & BHARATHI, M.C. 2021 Boundary-layer flow of the power-law fluid over a moving wedge: a linear stability analysis. *Engng Comput.* **37**, 1807–1820.
KUMBÁR, V., KOURILOVÁ, V., DUFKOVÁ, R., VOTAVA, J. & HRIVNA, L. 2021 Rheological and pipe flow properties of chocolate masses at different temperatures. *Foods* **10**, 2519.
LEVI, E. 1965 *Mecánica de los Fluidos: Introducción Teórica a la Hidráulica Moderna*. UNAM.
LONGO, S. 2011 Roll waves on a shallow layer of a dilatant fluid. *Eur. J. Mech. B/Fluids* **30** (1), 57–67.
LONGO, S., DI FEDERICO, V., ARCHETTI, R., CHIAPPONI, L., CIRIELLO, V. & UNGARISH, M. 2013 On the axisymmetric spreading of non-Newtonian power-law gravity currents of time-dependent volume: an experimental and theoretical investigation focused on the inference of rheological parameters. *J. Non-Newtonian Fluid Mech.* **201**, 69–79.
MARCHI, E. 1988 Correnti veloci in curve a 90° molto strette. *Idrotecnica* **14** (6), 439–455.
MARSDEN, J.E. & HUGHES, T.J.R. 1994 *Mathematical Foundations of Elasticity*. Dover Publications, Inc.
MATHIJSSEN, A.J.T.M., LISICKI, M., PRAKASH, V.N. & MOSSIGE, E.J.L. 2023 Culinary fluid mechanics and other currents in food science. *Rev. Mod. Phys.* **95** (2), 025004.
MUCHIRI, D.K., MONNIER, J. & SELLIER, M. 2025 Derivation and numerical resolution of 2D shallow water equations for multi-regime flows of Herschel–Bulkley fluids. *Eur. J. Mech. B/Fluids* **109**, 22–36.
NG, C.O. & MEI, C.C. 1994 Roll waves on shallow layer of mud modelled as a power-law fluid. *J. Fluid Mech.* **263**, 151–183.
NOBLE, P. & VILA, J.P. 2013 Thin power-law film flow down an inclined plane: consistent shallow-water models and stability under large-scale perturbations. *J. Fluid Mech.* **735**, 29–60.
OSHER, S. & FEDKIW, R.P. 2001 Level set methods: an overview and some recent results. *J. Comput. Phys.* **169** (2), 463–502.
POGGI, B. 1956 Correnti veloci nei canali in curva. *L'Energia Elettrica* **33**, 465–480.
PRANDTL, L. 1931, *Abriß der Strömungslehre*. Vieweg.
PREISWERK, E. 1938 *Anwendung Gasdynamischer Methoden auf Wasserströmungen mit freier Oberfläche*. ETH.
PRESS, H. & SCHRÖDER, R. 1966 *Hydromechanik im Wasserbau*. Verlag von Wilhelm Ernst & Sohn.

RAMASWAMY, B. & KAWAHARA, M. 1987 Lagrangian finite element analysis applied to viscous free surface fluid flow. *Intl J. Numer. Meth. Fluids* **7**, 953–984.
REINAUER, R. & HAGER, W.H. 1997 Supercritical bend flow. *J. Hydraul. Engng* **123** (3), 208–218.
RIABOUCHINSKY, D. 1932 Sur l'analogie hydraulique des mouvements d'un fluide compressible, *C. R. Acad. Sci. Paris* **195**, 998–999.
RIABOUCHINSKY, D. 1934 Sur l'analogie hydraulique des mouvements d'un fluide compressible. *C. R. Acad. Sci. Paris* **199**, 632–634.
ROUSE, H. 1938 *Fluid Mechanics for Hydraulic Engineers*. McGraw-Hill.
ROUSE, H. 1959 *Advanced Mechanics of Fluids*. Wiley.
RUYER-QUIL, C. & MANNEVILLE, P. 1998 Modeling film flows down inclined plane. *Eur. Phys. J. B - Condens. Matt. Complex Syst.* **6**, 277–298.
RUYER-QUIL, C. & MANNEVILLE, P. 2000 Improved modeling of flows down inclined plane. *Eur. Phys. J. B - Condens. Matt. Complex Syst.* **15**, 357–369.
RUYER-QUIL, C., CHAKRABORTY, S. & DANDAPAT, B.S. 2012 Wavy regime of a power-law film flow. *J. Fluid Mech.* **692**, 220–256.
SAMANTA, B., RAY, S., KAUSHAL, M. & DAS, G. 2022 Laminar planar hydraulic jump in thin film flow of power-law liquids - experimental analytical and numerical study. *Phys. Fluids* **34**, 103110.
SAMANTA, B., KAUSHAL, M., DAS, G. & RAY, S. 2023 Analysis of natural planar jump in power-law liquids - a generalized 'shallow-flow' approach. *Phys. Fluids* **35**, 113107.
SAMANTA, B., DAS, G., RAY, S. & KAUSHAL, M. 2024*a* Laminar planar hydraulic jump during free surface flow of Bingham plastic liquid. *Chem. Engng Sci.* **284**, 119505.
SAMANTA, B., KAUSHAL, M., DAS, G. & RAY, S. 2024*b* A numerical investigation of laminar planar hydraulic jump in Herschel–Bulkley fluid. *J. Non-Newtonian Fluid Mech.* **333**, 105325.
SANANES, F. & ACATAY, T. 1962 Contribution à l'étude des ècoulements supercritiques dans des canaux coudés. *C. R. Acad. Sci. Paris* **255**, 471–473.
SHU, J. & ZHOU, J. 2006 Characteristics of a hydraulic jump in Bingham fluid. *J. Hydraul. Res.* **44** (3), 421–426.
SOLARI, L. & DEY, S. 2016 Marchi's research on supercritical flow in tight bends and backwater effects. *J. Hydraul. Engng* **142**, 2.
UGARELLI, R. & DI FEDERICO, V. 2007 Transition from supercritical to subcritical regime in free surface flow of yield stress fluids. *Geographical Res. Lett.* **34**, 21.
VON KÁRMÁN, T. 1938 Eine praktische Anwendung der Analogie zwischen Überschallströmung in Gasen und überkritischer Strömung in offenen Gerinnen. *Z. Angew. Math. Mech.* **18** (1), 49–56.
WANG, W., KHAYAT, R.E. & DE BRUIN, J.R. 2023 The viscoplastic circular hydraulic jump. *Phys. Fluids* **35**, 063115.
WEISSTEIN, E.W. 1998 *CRC Concise Encyclopedia of Mathematics*. CRC Press.
WIELAND, M., GRAY, J.M.N.T. & HUTTER, K. 1999 Channelized free-surface flow of cohesionless granular avalanches in a chute with shallow lateral curvature. *J. Fluid Mech.* **392**, 73–100.
YU, B. & CHU, V.H. 2022 Impact of mud flow instabilities on hydraulic structures. In *Proceedings of the River Flow 2022 Conference*, vol. 1, pp. 1–2. CRC Press.
ZHANG, X., BAI, Y. & NG, C.O. 2020 Rheological properties of some marine muds dredged from China coasts. In *Proceedings of the* 28^{th} *International Offshore and Polar Engineering Conference*, pp. 455–461. ISOPE.
ZHOU, J.G., SHU, J.-J. & STANSBY, P.K. 2007 Hydraulic jump analysis for a Bingham fluid. *J. Hydraul. Res.* **45** (4), 555–562.